Shock dynamics in granular chains: numerical simulations and comparison with experimental tests

Ngoc-Son Nguyen, Bernard Brogliato

INSTITUT NATIONAL DE RECHERCHE EN INFORMATIQUE ET EN AUTOMATIQUE

Shock dynamics in granular chains: numerical simulations and comparison with experimental tests

Ngoc-Son Nguyen — Bernard Brogliato

N° 7636

May 2011

Modeling, Optimization, and Control of Dynamic Systems

Rapport de recherche

ISSN 0249-6399 ISRN INRIA/RR--7636--FR+ENG

INSTITUT NATIONAL
DE RECHERCHE
EN INFORMATIQUE
ET EN AUTOMATIQUE

INRIA

centre de recherche
GRENOBLE - RHÔNE-ALPES

Shock dynamics in granular chains: numerical simulations and comparison with experimental tests

Ngoc-Son Nguyen *, Bernard Brogliato †

Theme : Modeling, Optimization, and Control of Dynamic Systems
Équipes-Projets Bipop

Rapport de recherche n° 7636 — May 2011 — 62 pages

Abstract: The aim of this work is to simulate shock dynamics in granular chains of balls using the LZB multiple impact model and compare the numerical results to the experimental results available in the literature. The LZB model has been introduced to solve the multiple impact problem that arises in the rigid body systems when multiple contacts collide at the same time. The Darboux-Keller dynamics is considered in this model to change the time scale to the impulse scale. The interaction at the contact points is modeled by compliance contact laws. The energy dissipation at the contact points during the impact process, resulting from complex phenomena such as the plasticity, the viscosity, the noise, the vibration, etc., is taken into account by using Stronge's energetic coefficient of restitution. The coupling between various contact points, due to the wave effects, is described by a distributing law that relates the impulse change at one contact to that at another contact depending on their relative stiffness and their relative potential energy. The LZB model is then coupled to the event-driven scheme in order to simulate the motion of the nonsmooth mechanical systems. Different kinds of granular chains are investigated: monodisperse chains, *i.e.* chains of identical balls; tapered chains, *i.e.* chains composed of balls with decreasing size; stepped chains, *i.e.* chains composed of a large monodisperse section followed by a small monodisperse section. Particular attention is paid to the dispersion effect and the wave propagation in the tapered chains, to the interaction of two solitary waves in the monodisperse chains, and to the formation of a solitary wave train (a set of single solitary waves with decreasing amplitudes) in the stepped chains. Comparison with the experimental results shows that the numerical simulations with the LZB multiple impact model reproduce very well the experimental observations.

* INRIA, Bipop Team-Project, ZIRST Montbonnot, 655 Avenue de l'Europe, 38334 Saint Ismier, France; ngoc-son.nguyen@inrialpes.fr
† INRIA, Bipop Team-Project, ZIRST Montbonnot, 655 Avenue de l'Europe, 38334 Saint Ismier, France; bernard.brogliato@inrialpes.fr

Centre de recherche INRIA Grenoble – Rhône-Alpes
655, avenue de l'Europe, 38334 Montbonnot Saint Ismier
Téléphone : +33 4 76 61 52 00 — Télécopie +33 4 76 61 52 52

Key-words: Multiple impacts, LZB model, Event-Driven Scheme, Monodisperse Chain, Tapered Chain, Stepped Chain

Dynamique de choc dans des chaînes granulaires: simulations numériques et comparaison avec des tests expérimentaux

Résumé : L'objectif de ce travail est de simuler la dynamique de choc dans des chaînes granulaires en considérant le modèle LZB puis de comparer les résultats numériques avec les résultats expérimentaux existant dans la littérature. Le modèle LZB a été introduit pour résoudre le problème d'impacts multiples rencontré pour les systèmes multicorps rigides lorsque les chocs se produisent simultanément à plusieurs contacts. Pour ce modèle, la dynamique de Darboux-Keller est utilisée pour changer l'échelle du temps en l'échelle de l'impulsion. L'interaction aux points de contact est modélisée par des lois de contact de type compliance. La dissipation de l'énergie aux points de contact, due à des phénomènes physiques complexes comme la plasticité, la viscosité, le bruit, la vibration, etc., est prise en compte par un coefficient de restitution énergétique. Le couplage entre plusieurs points de contact, dû aux effets d'onde, est décrit par une loi de distribution qui relie le changement de l'impulsion à un contact à celui à un autre contact en fonction de leur rigidité relative et de leur énergie potentielle relative. Le modèle LZB est ensuite couplé à une méthode numérique "event-driven" pour simuler le mouvement des systèmes mécaniques non-réguliers. Differents types de chaîne granulaire sont étudiés: chaînes monodisperses, *i.e.* chaînes composées de billes identiques; chaînes "tapered", *i.e.* chaînes composées de billes de taille décroissante; chaînes "stepped", *i.e.* chaînes composées d'une section monodisperse à grand rayon puis d'une section monodisperse à petit rayon. On s'intéresse particulièrement à l'effet de dispersion et la propagation de l'onde dans les chaînes "tapered", à l'interaction de deux ondes solitaires dans les chaînes monodisperses, à la formation d'un train d'ondes solitaires (un ensemble d'ondes solitaires individuelles avec amplitudes décroissantes) dans les chaînes "stepped". La comparaison avec les résultats expérimentaux montre que les simulations numériques avec le modèle LZB reproduisent de façon très statisfaisante les observations expérimentales.

Mots-clés : Impacts Multiples, Modèle LZB, Méthode Event-Driven, Chaîne Granulaire

Contents

1 Introduction

The dynamics of chains of balls subjected to collisions has been the object of many studies since a long time, the most well-known example being the so-called Newton's cradle (see *e.g.* [1, §6.5.6] for references). Chains of balls are of interest for researchers in Solid Mechanics because it is a nice example of a system with *multiple impacts* (the system is subject to several simultaneous impacts), and for researchers in Physics because it is the simplest example of a granular material. Multiple impacts are known to be a challenging issue in the impact modeling, even for frictionless impacts (like in chains of aligned balls) [13, 22]. Despite their apparent simplicity chains of balls possess a quite complex collision dynamics that involves two main physical effects: dissipation and dispersion of energy. The dissipation is mainly due to the local deformation at the contact/impact areas and may have many sources: viscosity, plasticity, sound, hysteretic effects, *etc.* The dispersion rather quantifies the way the initial energy of the chain (before the impact) is spread within the chain after the impact has occurred. The waves effets are responsible for the dispersion, which occurs even if the dissipation is almost zero (conservative system). For this reason waves phenomena have been analyzed a lot [20, 23]. The dissipation may have, on the other hand, an influence on the dispersion.

Obtaining good models of multiple impacts with good numerical methods is an important issue in the field of granular matter in general, and for chains of balls as a particular case. Models based on kinematic restitution coefficients (Newton's like) or on kinetic restitution coefficients (Poisson's like) are known not to be rich enough to correctly represent the dispersion effects. Moreover they present serious deficiencies like non-uniqueness of the restitution coefficients for a given energetic behaviour, or the necessity to estimate the restitution matrix for each chain and each initial data. Other models based on Routh's impact dynamics [1, §4.2.13] and an impulse correlation ratio (ICR) have been proposed [5, 12]. However it seems that the assumption that the ICR can be estimated from experiments between triplets of balls may fail [22, §6.4]. Let us mention that kinematic laws and binary collisions (the contact gaps are assumed to be all open) are sometimes used [40, 42, 44, 43]. This is also prone to some fundamental issues like the fact that it is not guaranteed, in general, that letting the gaps tend to zero (hence recovering the real system where the balls touch each other) yield a unique limit, because the trajectories may be discontinuous with respect to the initial data [21]. In order to take into account the local dissipation at contact points during the impact process, several works introduced viscous dissipation with linear or nonlinear viscosity coupled to Hert's contact law [37, 38, 14]. This viscous dissipation model might be valid for the viscous elastic material but it cannot take into account some important effects like plasticity, dissipation due to the noise, light, vibration, etc. In [39, 48], the local dissipation at contact points is modeled by a coefficient of restitution defined as the ratio of the unloading force (during the expansion phase) to the loading force (during the compression phase). This restitution law is quite simple, however most materials do not show such a restitution law. It happens that dissipation at contact points is a complex phenomenon, that can be hardly be encapsulated by the models mentioned above. One contribution of this paper and former ones [15, 16, 17, 25, 24] is to introduce an energetic coefficient of restitution, instead.

Granular chains has attracted much attention of scientists in investigating the energy propagation in such discrete media in order to find out shock protection devices that are able to attenuate efficiently the energy induced in a shock process. Various kinds of granular chains have been investigated:

- monodisperse chains, *i.e.* chains of identical balls [11, 23, 2, 14, 32, 37];
- monodisperse chains with defects [9, 49];
- tapered chains, *i.e.* chains with decreasing size of the balls [45, 46, 48, 42, 40, 47];
- stepped chains, *i.e.* chains composed of a large monodisperse section followed by a small monodisperse section [30, 33, 28];
- decorated chains with small masses placed regularly or randomly among larger masses [44, 43, 12];
- composite chains, *i.e.* chains composed of beads made of different materials periodically or randomly distributed [7, 8, 6, 29, 38];
- disordered chains with beads of masses randomly distributed [41, 39].

The subject of this paper is the study of the dispersion effect and the wave propagation in the tapered chains, of the formation of the solitary wave trains in the stepped chains and of the interaction of two solitary waves in the monodisperse chains. More specifically the multiple impact model introduced in [15, 16, 17] (and called in the sequel the LZB-complementarity multiple impact model) is used and the numerical results are carefully compared to experimental data available in [19, 18, 30, 32]. Comparisons between numerical results obtained with the LZB multiple impact model coupled to a complementarity model outside the impacts in an event-driven method, and experimental data have been presented in [16] for column of beads (experiments of [11]), in [25] for the bouncing dimer (experiments of [10]), Newton's cradle in [17] (experiments of [5]), and more recently some results on the rocking block system used in the Earthquake Engineering literature [24].

This paper is organized as follows: in section 2, we will present briefly the LZB multiple impact model coupled to the event-driven numerical scheme. In section 3, granular chains and their dynamics will be described. Section 4 and 5 will be dedicated to investigate the dispersion effect and the wave propagation in the tapered chains and compare the numerical results to the experimental results presented in [19] and [18]. The formation of solitary wave trains in the stepped chains will be the subject of section 6, and the numerical results will be compared to the experimental ones shown in [30]. In section 7, the numerical simulations concerning the interaction of two solitary waves in the monodisperse chains will be presented and compared to the experimental data available in [32]. Finally, some conclusions about the numerical simulations with the LZB multiple impact model will be drawn.

2 Event-driven scheme and LZB-complementarity model

In this section we summarize the event-driven scheme used to solve the dynamics of a multiple rigid body system with the LZB-comlementarity multiple impact model. This means that the whole motion of the system is solved with the event-driven scheme during which some singular points happen (impact between rigid bodies), and the LZB-complementarity model is applied to solve these singular points. For the sake of simplicity, we limit ourselves to the case without friction. For this case, the event-driven scheme and the LZB-complementarity impact model, that will be described below, have been implemented in the SICONOS platform and are available at `http://siconos.gforge.inria.fr`.

Let us consider a multiple rigid body system with s possible frictionless contact points. The maximum number of degrees of freedom (obtained when none of contacts is closed) is n. The state of the system may be described by a set of generalized coordinates $\boldsymbol{q} \in \mathbb{R}^n$. The dynamics of this nonsmooth system can be described by the equation of motion and a set of complementarity conditions as follows:

$$\begin{cases} \boldsymbol{M}(\boldsymbol{q}(t))\ddot{\boldsymbol{q}}(t) + \boldsymbol{F}_{int}(t, \boldsymbol{q}(t), \dot{\boldsymbol{q}}(t)) = \boldsymbol{F}_{ext}(t) + \boldsymbol{W}(\boldsymbol{q}(t))\boldsymbol{\lambda}(t) \\ 0 \leq \boldsymbol{\lambda}(t) \perp \boldsymbol{\delta}(\boldsymbol{q}(t)) \geq 0, \end{cases} \tag{1}$$

where:

- $\boldsymbol{M}(\boldsymbol{q}(t)) \in \mathbb{R}^{n \times n}$ is the inertia matrix;
- $\boldsymbol{\delta}(\boldsymbol{q}(t)) = [\delta_1(\boldsymbol{q}(t))\ \delta_2(\boldsymbol{q}(t))...\delta_s(\boldsymbol{q}(t))]^T$ and $\boldsymbol{\lambda}(t) = [\lambda_1(t)\ \lambda_2(t)...\lambda_s(t)]^T$ with $\delta_j(\boldsymbol{q}(t))$ and $\lambda_j(t)$ being the gap and the force at contact point j, respectively;
- $\boldsymbol{F}_{int}(t, \boldsymbol{q}(t), \dot{\boldsymbol{q}}(t))$ collects the nonlinear terms resulting from the nonlinear inertial terms, the nonlinear interactions between bodies, and $\boldsymbol{F}_{ext}(t)$ is the external loading;
- $\boldsymbol{W}(\boldsymbol{q}(t)) \in \mathbb{R}^{n \times s}$ is the Jacobian matrix:

$$\boldsymbol{W}(\boldsymbol{q}(t))^T = \frac{\partial \boldsymbol{\delta}(\boldsymbol{q}(t))}{\partial \boldsymbol{q}(t)}. \tag{2}$$

In order to establish the algorithm for the event-driven scheme and for the LZB-complementarity multiple impact model, three index sets have been introduced in [35] for the case without friction at the contacts as follows:

- The index set I is the set of all possible contact points in the system:

$$I = \{1, 2, ..., s\} \subset \mathbb{N}; \tag{3}$$

- The index set I_c is the set of all closed contacts of the system:

$$I_c = \{j \in I \mid \delta_j(\boldsymbol{q}(t)) = 0\} \subset I; \tag{4}$$

- The index set I_s is the set of all persistent contacts (rolling or sliding contacts) in the system:

$$I_s = \{j \in I_c \mid \dot{\delta}_j(\boldsymbol{q}(t)) = 0\} \subset I_c. \tag{5}$$

First of all, we talk about how the impact problem is solved with the LZB-complementarity impact model. Lastly, we describe the event-driven scheme associated with the LZB-complementarity impact model.

2.1 LZB-complimentarity multiple impact model

Let us consider the case when the nonsmooth system described above is subjected to a multiple impact process. At this instant, there are m active contact points in the system (the contacts belong to the index set $I_c \subset I$). The LZB-complementarity multiple impact model to solve the impact problem for this case is summarized below. The numerical scheme for this model is described in the appendix A.

1) The configuration $\boldsymbol{q} \in \mathbb{R}^n$ of the system is assumed to be constant during the impact process, and so are $\boldsymbol{M}(\boldsymbol{q})$ and $\boldsymbol{W}(\boldsymbol{q})$. Therefore, the Darboux-Keller's dynamical equation [3, 4] is used to change the time scale to the impulse scale, as follows:

$$\boldsymbol{M}(\boldsymbol{q})\frac{d\dot{\boldsymbol{q}}}{dP_*} = \boldsymbol{W}_c(\boldsymbol{q})\frac{d\boldsymbol{P}}{dP_*}, \tag{6}$$

where:

- The Jacobian matrix $\boldsymbol{W}_c(\boldsymbol{q}) \in \mathbb{R}^{n\times m}$ is related to only the index set I_c. The connection between the relative velocity at the active contact points $\dot{\boldsymbol{\delta}} \in \mathbb{R}^m$ and the generalized velocity $\dot{\boldsymbol{q}} \in \mathbb{R}^n$ is given by:

$$\dot{\boldsymbol{\delta}}(\boldsymbol{q}) = \boldsymbol{W}_c(\boldsymbol{q})^T\dot{\boldsymbol{q}}. \tag{7}$$

  The convention made for the relative velocity at contact point j as follows: $\dot{\delta}_j > 0$ for two colliding bodies approaching (compression phase) and $\dot{\delta}_j < 0$ for the separation (expansion phase);

- $d\boldsymbol{P} \in \mathbb{R}^m$ is the change of the normal impulse at the active contact points;

- dP_* is an independent time-like variable defined at the velocity-impulse level and called "the principal impulse".

From (6) and (2), we have:

$$\frac{d\dot{\boldsymbol{\delta}}}{dP_*} = \boldsymbol{W}_c(\boldsymbol{q})^T\boldsymbol{M}(\boldsymbol{q})^{-1}\boldsymbol{W}_c(\boldsymbol{q})\frac{d\boldsymbol{P}}{dP_*} = \boldsymbol{H}(\boldsymbol{q})\frac{d\boldsymbol{P}}{dP_*}, \tag{8}$$

where $\boldsymbol{H}_c(\boldsymbol{q}) = \boldsymbol{W}_c(\boldsymbol{q})^T\boldsymbol{M}(\boldsymbol{q})^{-1}\boldsymbol{W}_c(\boldsymbol{q})$.

2) The interaction at contact points is modeled by a compliant contact model that may be a mono-stiffness or a bi-stiffness model as described below:

- the mono-stiffness compliant model expresses the same force λ_j/identation δ_j mapping at contact point j for the compression phase and the expansion phase:

$$\lambda_j = K_j(\delta_j)^\eta, \tag{9}$$

where K_j is the stiffness at contact point j and η is the elasticity coefficient ($\eta = \frac{3}{2}$ for the Hertz contact model and $\eta = 1$ for the linear elastic model).

- the bi-stiffness compliant model makes the force/identation mapping for the compression phase different from the one for the expansion phase as shown in figure 1. The force/identation mapping for this model is:

$$\begin{aligned} \lambda_{c,j} &= K_j(\delta_j)^\eta && \text{for compression phase,} \\ \lambda_{e,j} &= \lambda_{M,j}\Big(\frac{\delta_j - \delta_{r,j}}{\delta_{M,j} - \delta_{r,j}}\Big)^\eta && \text{for expansion phase,} \end{aligned} \tag{10}$$

where $\delta_{r,j}$ is the plastic deformation, and $\lambda_{M,j}$ and $\delta_{M,j}$ are the maxima of the normal contact force and normal deformation at the end of the compression phase (when $\dot{\delta}_j = 0$).

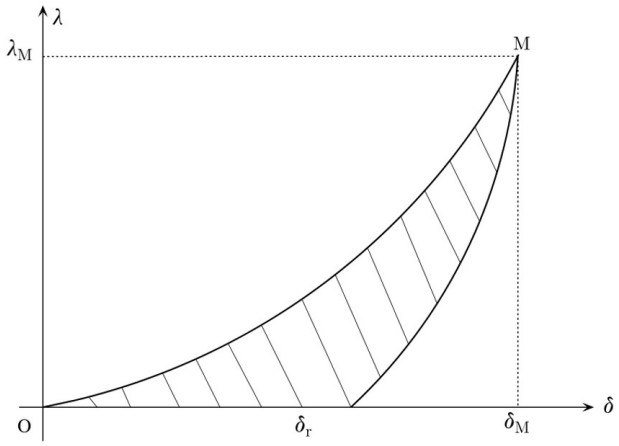

Figure 1: Bi-stiffness contact compliant model.

3) A distributing law relating the change of the impulse (dP_j) at contact j to the change of the impulse (dP_*) at the so-called primary contact, which is defined as the contact where the potential energy is maximum, can be derived from the compliant contact models presented above. The distributing rule has the following form:

$$\frac{dP_j}{dP_*} = \gamma_{j,*}^{\frac{1}{1+\eta}} (E_{j,*}(P_j, P_*))^{\frac{\eta}{\eta+1}}, \tag{11}$$

where $\gamma_{j,*} = \dfrac{K_j}{K_*}$ and $E_{j,*}(P_j, P_*) = \dfrac{E_j(P_j)}{E_*(P_*)}$ are respectively the ratios of the stiffness and the potential energy at contact j to those at the primary contact. Some singularities arise during an impact process, for which the distributing rule shown in (11) becomes invalid. One singularity is encountered at the beginning of the impact process when the potential energy is zero at any contact. In this

case, a distributing rule should be derived in terms of relative velocity at contact points and has the following form

$$\frac{dP_j}{dP_*} = \gamma_{j,*}\Big(\frac{\dot{\delta}_j}{\dot{\delta}_*}\Big)^{\eta}. \tag{12}$$

The primary contact in this case is defined as the contact where the relative velocity is maximum. During the impact process it is possible that a contact does not participate into the impact at an instant P and then participates again into the impact at the following instants, due to the constraints between the neighboring particles. In such a case, an approximated distributing rule can be derived as follows:

$$\frac{dP_j}{dP_*} = \gamma_{j,*}\Big(\frac{\dot{\delta}_j dP_*}{E_*}\Big)^{\eta}. \tag{13}$$

4) The local dissipation due to the inelastic interactions at contact points is taken into account by using the energetic constraint introduced in [26]

$$e_{s,j}^2 = -\frac{W_{e,j}}{W_{c,j}} = \frac{\int_{P_j^c}^{P_j^f} \dot{\delta}_j(P_j)dP_j}{\int_0^{P_j^c} \dot{\delta}_j(P_j)dP_j}, \tag{14}$$

where $W_{c,j}$ and $W_{e,j}$ are respectively the works done by the contact force at contact j during the compression phase and the expansion phase. The instant P_j^c is determined when $\dot{\delta}_j(P_j^c) = 0$ and P_j^f corresponds to the instant when the expansion phase is terminated. The enegetic constraint introduces a parameter named *the energetic restitution coefficient* e_s.

It is worth noting that the local dissipation is not included in the mono-stiffness model. So in order to satisfy the energetic constraint, when condition (14) is achieved, the residual potential energy will be discarded (the residual potential energy is set to zero when condition (14) is achieved). Physically speaking, the mechanism used to dissipate the energy in the mono-stiffness model is not clear. In contrast, the local dissipation for the elasto-plastic materials is consistently included in the bi-stiffness model and the dissipative parameters in this model are related to the energetic restitution coefficient by the relation $\delta_{r,j} = \delta_{M,j}(1 - e_{s,j}^2)$.

5) The potential energy at a contact is computed as follows:

- For the mono-stiffness model:

$$E_j(P_j) = \int_0^{P_j} \dot{\delta}_j(P_j)dP_j, \tag{15}$$

  for the compression and expansion phases. In accordance with the energetical constraint (14) when the potential energy $E_j(P_j)$ satisfies $E_j(P_j) = W_{c,j}(1 - e_{s,j}^2)$, the residual potential energy will be completely dissipated. This means that when $E_j(P_j) = W_{c,j}(1-e_{s,j}^2)$, the potential energy $E_j(P_j)$ must be set to zero.

- For the bi-stiffness model:

$$\begin{aligned} E_j(P_j) &= \int_0^{P_j} \dot{\delta}_j(P_j)dP_j && \text{for compression phase,} \\ E_j(P_j) &= \int_0^{P_j^c} \dot{\delta}_j(P_j)dP_j + \frac{1}{e_{s,j}^2}\int_{P_j^c}^{P_j} \dot{\delta}_j(P_j)dP_j && \text{for expansion phase.} \end{aligned} \tag{16}$$

6) The force at contact point j is computed from the potential energy as follows:

$$\lambda_j = (1+\eta)^{\frac{\eta}{\eta+1}} K_j^{\frac{1}{1+\eta}} (E_j(P_j(t)))^{\frac{\eta}{\eta+1}}, \tag{17}$$

and the time scale t is related to the principal impulse scale P_* (impulse at the primary contact point) by the following relation:

$$dt = \frac{dP_*}{F_*}, \tag{18}$$

where F_* is the force computed at the primary contact point using (17).

7) The impact at a contact is considered to be terminated if the residual potential energy at the contact is completely released during the expansion phase. This means that the following condition must be satisfied

$$E_j = 0 \text{ and } \dot{\delta}_j \leq 0. \tag{19}$$

The multiple impact process is considered to be terminated if the impact at all the contacts of the system is terminated.

2.2 Event-driven scheme

During the motion of the system described in (1), some nonsmooth events might happen when some of contacts are activated (rigid bodies at the active contacts collide each other). Between the nonsmooth events, the motion of the system is smooth. The event-driven scheme to solve the system (1) consists in integrating the smooth motion between two nonsmooth events and in processing the nonsmooth motion when a nonsmooth event is encountered. The crutial point in this numerical scheme is that the nonsmooth events have to be efficiently localized.

When the set of active contacts $I_c = \emptyset$, no contact is activated in the system. So there is no force at any contact and system (1) becomes:

$$\begin{cases} \boldsymbol{M}(\boldsymbol{q}(t))\ddot{\boldsymbol{q}}(t) + \boldsymbol{F}_{int}(t, \boldsymbol{q}(t), \dot{\boldsymbol{q}}(t)) = \boldsymbol{F}_{ext}(t) \\ \delta_j(\boldsymbol{q}(t)) > 0 \ \forall j \in I. \end{cases} \tag{20}$$

Equation (20) is an Ordinary Differential Equation (ODE) subjected to a set of unilateral contraints $\delta_j(\boldsymbol{q}(t)) > 0 \ \forall j \in I$ and can be efficiently solved by various numerical schemes proposed in the litterature. One of them is the DLSODAR solver [34]. Furthermore, this solver allows to detect efficiently the instants when some unilateral constraints are violated. Therefore, the nonsmooth events when some contact points are activated (when $\delta_j = 0$) can be efficiently localized.

When $I_c \neq \emptyset$ and $I_c \setminus I_s \neq \emptyset$, some contacts in the system come into collision. A nonsmooth event is encountered and needs to be processed by a nonsmooth

law. Here we use LZB-complementarity multiple impact model to process the nonsmooth event encountered. Such a nonsmooth event processing has been described in section 2.1.

When $I_c \neq \emptyset$ and $I_c \setminus I_s = \emptyset$, all the active contacts in the system are persistent contacts (sliding or rolling contacts). The motion of the sytem in this case is smooth. This motion can be solved by reformulating the complementarity conditions in (1) at the acceleration level. System (1) can be rewritten as follows:

$$\begin{cases} \boldsymbol{M}(\boldsymbol{q}(t))\ddot{\boldsymbol{q}}(t) + \boldsymbol{F}_{int}(t, \boldsymbol{q}(t), \dot{\boldsymbol{q}}(t)) = \boldsymbol{F}_{ext}(t) + \boldsymbol{W}(\boldsymbol{q}(t))\boldsymbol{\lambda}(t) \\ \lambda_j(t) = 0 \quad \forall j \in I \setminus I_s \\ 0 \leq \lambda_j(t) \perp \ddot{\delta}_j(\boldsymbol{q}(t)) \geq 0 \quad \forall j \in I_s. \end{cases} \tag{21}$$

We have:

$$\begin{aligned} \ddot{\boldsymbol{\delta}}(\boldsymbol{q}(t)) &= \boldsymbol{W}^T(\boldsymbol{q}(t))\ddot{\boldsymbol{q}}(t) + \dot{\boldsymbol{W}}^T(\boldsymbol{q}(t))\dot{\boldsymbol{q}}(t) \\ &= [\boldsymbol{W}^T(\boldsymbol{q}(t))\boldsymbol{M}^{-1}(\boldsymbol{q}(t))\boldsymbol{W}(\boldsymbol{q}(t))]\boldsymbol{\lambda}(t) + \boldsymbol{W}^T(\boldsymbol{q}(t))\boldsymbol{M}^{-1}(\boldsymbol{q}(t))[\\ &\boldsymbol{F}_{ext}(t) - \boldsymbol{F}_{int}(t, \boldsymbol{q}(t), \dot{\boldsymbol{q}}(t))] + \dot{\boldsymbol{W}}^T(\boldsymbol{q}(t))\dot{\boldsymbol{q}}(t) \\ &= \boldsymbol{H}(\boldsymbol{q}(t))\boldsymbol{\lambda}(t) + \boldsymbol{\beta}(t, \boldsymbol{q}(t), \dot{\boldsymbol{q}}(t)), \end{aligned} \tag{22}$$

where:

$$\boldsymbol{H}(\boldsymbol{q}(t)) = \boldsymbol{W}^T(\boldsymbol{q}(t))\boldsymbol{M}^{-1}(\boldsymbol{q}(t))\boldsymbol{W}(\boldsymbol{q}(t)), \tag{23}$$

$$\boldsymbol{\beta}(t, \boldsymbol{q}(t), \dot{\boldsymbol{q}}(t)) = \boldsymbol{W}^T(\boldsymbol{q}(t))\boldsymbol{M}^{-1}\boldsymbol{q}(t))[\boldsymbol{F}_{ext}(t) - \boldsymbol{F}_{int}(t, \boldsymbol{q}(t), \dot{\boldsymbol{q}}(t))] + \dot{\boldsymbol{W}}^T(\boldsymbol{q}(t))\dot{\boldsymbol{q}}(t). \tag{24}$$

Combining (21) and (22) and, we obtain:

$$\boldsymbol{M}(\boldsymbol{q}(t))\ddot{\boldsymbol{q}}(t) + \boldsymbol{F}_{int}(t, \boldsymbol{q}(t), \dot{\boldsymbol{q}}(t)) = \boldsymbol{F}_{ext}(t) + \boldsymbol{W}(\boldsymbol{q}(t))\boldsymbol{\lambda}(t), \tag{25}$$

$$\begin{cases} \ddot{\boldsymbol{\delta}}(\boldsymbol{q}(t)) = \boldsymbol{H}(\boldsymbol{q}(t))\boldsymbol{\lambda}(t) + \boldsymbol{\beta}(t, \boldsymbol{q}(t), \dot{\boldsymbol{q}}(t)) \\ \lambda_j(t) = 0 \quad \forall j \in I \setminus I_s \\ 0 \leq \lambda_j(t) \perp \ddot{\delta}_j(\boldsymbol{q}(t)) \geq 0 \quad \forall j \in I_s. \end{cases} \tag{26}$$

It can be seen that system (26) is a linear complementarity problem (LCP) with contact force $\boldsymbol{\lambda}(t)$ as its unknown. This LCP can be solved by various numerical algorithms (for example, Lemke's algorithm described in [35]). The ODE (25) can be solved with an ODE solver, for example the DLSODAR solver. Systems (25) and (26) are solved by first solving the LCP (26) to determine the unknown $\boldsymbol{\lambda}(t)$, then updating and solving the ODE (25). During the integration of the ODE (25), the set of constraints $\delta_j(\boldsymbol{q}(t)) > 0 \quad \forall j \in I \setminus I_s$ and $\lambda_j(t) > 0 \quad \forall j \in I_s$ is checked and the nonsmooth events when some contact points are activated or desactivated (a contact point j is activated if $\delta_j(\boldsymbol{q}(t)) = 0$ and desactivated if $\lambda_j(t) = 0$) can be efficiently localized.

The algorithm for the event-driven scheme described above has been presented in [35] and is summarized in section B.

3 Numerical simulation of granular chains

In this section, we present the numerical simulation of the dynamics of granular chains by using the event-drivent scheme combined with the LZB-complementarity

multiple impact model presented in section 2.1. Figure 2 illustrates a granular chain. As illustrated in this figure, a granular chain is composed of beads whose center is aligned on a horizontal axis. This alignement aims at ensuring co-linear collisions between beads. Last bead in the chain may move freely or may be constraint by a rigid wall placed at the end of the chain. The beads in the chain are numbered as increasing integers from 1 for first bead to N for last bead (N is the number of beads in the chain). For a bead i, the position of its center is defined by x_i, and its radius is R_i. The chain is impacted by a bead (striker) numbered as 0 with an impact velocity V_s. In the case when there is no rotation of the beads, the state of the system (striker + chain) is described by the following generalized coordinate $\boldsymbol{q} = [x_0, x_1, ..., x_N]^T$. Let us assume that at the beginning of the impact process all the contacts in the chain are closed.

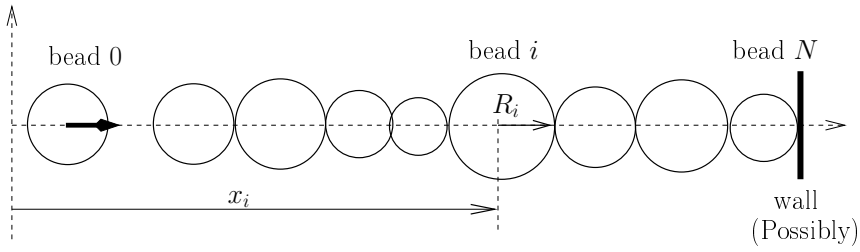

Figure 2: Configuration of a granular chain with possibly a rigid wall at the end impacted by a striker (bead 0).

The mass matrix for this chain is:

$$\boldsymbol{M} = \begin{bmatrix} m_0 & 0 & \cdots & 0 \\ 0 & m_2 & \cdots & 0 \\ \vdots & \vdots & \ddots & \vdots \\ 0 & 0 & \cdots & m_N \end{bmatrix}_{(N+1)\times(N+1)} . \tag{27}$$

Contact between bead i and bead $i+1$ is numbered as i and the contact between last bead and the wall is numbered as N. The gaps at the contacts are:

$$\begin{array}{l} \delta_i = x_{i+1} - x_i - (R_i + R_{i+1}) \ \ \forall i \neq N \\ \delta_N = x_{wall} - x_N - R_N. \end{array} \tag{28}$$

The matrix $\boldsymbol{W}_c$ ($\boldsymbol{W}_c = \left[\dfrac{\partial \boldsymbol{\delta}}{\partial \boldsymbol{q}}\right]^T$) for the case without wall is:

$$\boldsymbol{W}_c = \begin{bmatrix} -1 & 0 & 0 & \cdots & 0 \\ 1 & -1 & 0 & \cdots & 0 \\ 0 & 1 & -1 & & \vdots \\ \vdots & & \ddots & \ddots & 0 \\ 0 & 0 & 0 & 1 & -1 \\ 0 & 0 & 0 & 0 & 1 \end{bmatrix}_{(N+1)\times N} . \tag{29}$$

When the wall is present, the matrix $\boldsymbol{W}$ becomes:

$$\boldsymbol{W}_c = \begin{bmatrix} -1 & 0 & 0 & \cdots & 0 & 0 \\ 1 & -1 & 0 & \cdots & 0 & 0 \\ 0 & 1 & -1 & \ddots & \vdots & 0 \\ \vdots & \ddots & \ddots & \ddots & 0 & \vdots \\ 0 & 0 & 0 & 1 & -1 & 0 \\ 0 & 0 & 0 & 0 & 1 & -1 \end{bmatrix}_{(N+1)\times(N+1)} . \tag{30}$$

It is worth mentioning that both $\boldsymbol{M}$ and $\boldsymbol{W}_c$ are constant during the motion of the system so the Darboux-Keller basic assumption mentioned in section 2.1 is automatically satisfied for such chains of balls.

The dynamics of the chain is described by the following system:

$$\begin{cases} \boldsymbol{M}\ddot{\boldsymbol{q}}(t) = \boldsymbol{W}_c\boldsymbol{\lambda}(t) \\ 0 \leq \boldsymbol{\delta}(t) \perp \boldsymbol{\lambda}(t) \geq 0, \end{cases} \tag{31}$$

and the Darboux-Keller's equation when the impact occurs in the chain is:

$$\boldsymbol{M}d\dot{\boldsymbol{q}} = \boldsymbol{W}_c d\boldsymbol{P}. \tag{32}$$

The interaction between adjacent beads when they are in contact is modeled by either the mono-stiffness model (9) or the bi-stiffness model (10) and subjected to the energetical constraint (14). The stiffness at contact point i is computed according to the Hertz's theory:

$$K_i = \frac{4}{3}\sqrt{R_i^*}E_i^*, \tag{33}$$

where R_i^* and E_i^*

$$\begin{aligned} \frac{1}{R_i^*} &= \frac{1}{R_i} + \frac{1}{R_{i+1}} \\ \frac{1}{E_i^*} &= \frac{1-\nu_i^2}{E_i} + \frac{1-\nu_{i-1}^2}{E_{i+1}}, \end{aligned} \tag{34}$$

Here E_i and ν_i are the Young modulus and the Poisson coefficient of bead i. If the wall is at the end of the chain, R_N^* and E_N^* for the contact N between last bead and the wall is computed as follows:

$$\begin{aligned} R_N^* &= R_N \\ \frac{1}{E_N^*} &= \frac{1-\nu_N^2}{E_N} + \frac{1-\nu_w^2}{E_w}, \end{aligned} \tag{35}$$

with E_w and ν_w are the Young modulus and the Poisson coefficient of the wall.

The motion of the chain is simulated with the event-driven scheme described in section 2.2 and the impact process is solved with LZB-complementarity multiple impact model described in section 2.1. The choice of the step size ΔP to solve LZB-complementarity impact model for different granular chains is discussed in section A.2.

4 Simulations of the experimental test in [19]

4.1 Description of the experimental test

Nakagawa *et al.* [19] have conducted a series of experimental tests on a tapered chain of balls in order to investigate the dispersion effect in this kind of granular chain. The configuration of these experimental tests is illustrated in figure 3. The tapered chain is composed of 19 balls (numbered from 1 for the largest ball to 19 for the smallest ball) whose diameter Φ_i is progressively decreased according to the following law: $\Phi_i = (1-q)\Phi_{i-1}$ with $\Phi_1 = 9.5$ mm and the tapering factor $q = 5\%$. Initially, the balls in the tapered chain barely touch one another. The tapered chain is then impacted by an impactor (numbered 0) of diameter $\Phi_0 = 10$ mm and made of the same material as the balls in the tapered chain. The ball properties correspond to the steel properties as follows: mass density $\rho = 7833\text{kg/m}^3$, Young modulus $E = 203$ GPa, Poisson ratio $\nu = 0.3$. In order to estimate the restitution coefficient of the balls, the authors have perfomed binary collision experiments with pairs of balls of the same size. Three values are found for the restitution coefficient: 0.947, 0.965 and 0.955 corresponding to the values of the ball velocity averaged over 5 ms, 15 ms and 20 ms, respectively. The velocity of the balls at the end of the impact (defined at the moment when the smallest ball leaves the chain) is measured by a high-speed digital image analysis.

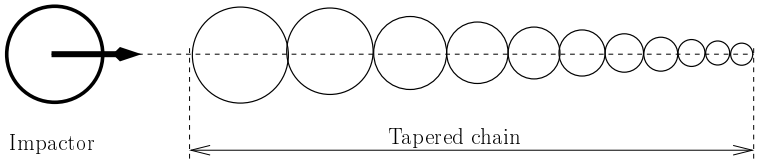

Figure 3: Configuration of the test of Nakagawa *et al.* [19].

4.2 Comparison between numerical and experimental results

We perform numerical simulations of the experimental tests presented above with the LZB-complementarity multiple impact model. The parameters for the ball properties used in the simulations are the same than those presented in section 4.1. The bi-stiffness compliance model is considered with an elasticity coefficient $\eta = 3/2$. Since there is not a unique value presented in [19] for the restitution coefficient, we choose to use the three values of 0.947, 0.965, 0.955 in the simulations and compare the numerical results obtained with these values. The simulations are performed with a step size $\Delta P = 10^{-6}\ N.s$.

In order to obtain the experimental data shown in a figure of a paper, we use the following data extracting technique. First the considered figure is extracted from an electronic version of the paper. Then we open the extracted figure by an image processing software to make the resolution of the figure high enough. The position of the interested point on the figure with respect to an origin point (with an arbitrary unit) is dertermined by measuring on the figure. Knowing

the value corresponding to the origin point and the scale of the figure allows to find the value that corresponds to the interested point by an interpolation or an extrapolation. In the case when the experimental data is shown with error bars, only the data concerning the central points which are obtained from statistical treatements are extracted. Figure 4 illustrates the result of the data extracting technique described above.

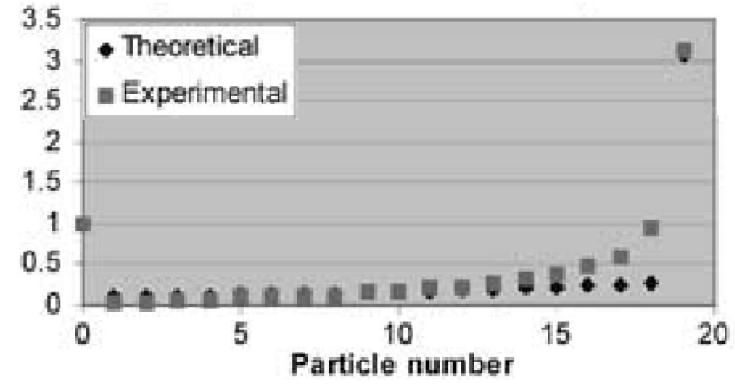

(a)

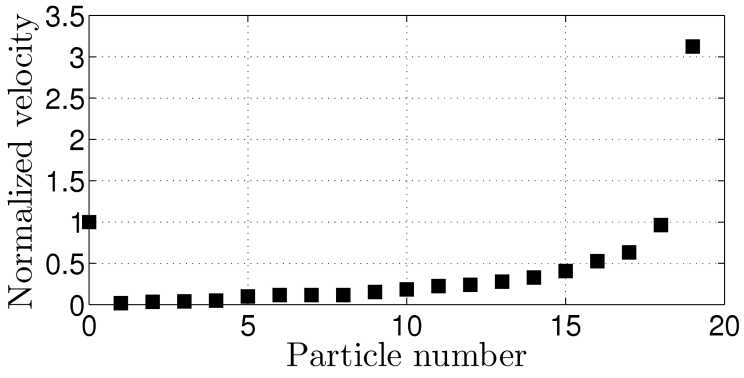

(b)

Figure 4: Illustration of the data extracting technique: (a) the original figure 6 shown in [19] and (b) figure shows the corresponding data extracted.

Figure 5 shows the post-impact velocity of the balls in the chain obtained from the numerical simulations with three values of the restitution coefficient (0.947, 0.965, 0.955), compared to the experimental results presented in [19]. It is shown that the numerical simulations give results that are close to the experimental results. The multiple impact law underestimates (resp. overestimates) slightly the post-impact velocity of the balls at the right end (resp. the left end) of the chain. Moreover, the numerical results obtained with the value of 0.965 for the restitution coefficient match the best the experimental ones. We will see in section 5.2 that such a value for the restitution coefficient is found by a fitting procedure to the experiments performed by Melo *et al.* [18]. The balls used in these tests are made of the same material as that of the balls used in

[19] (the ball properties: mass density, Young modulus, Poisson coefficient are the same).

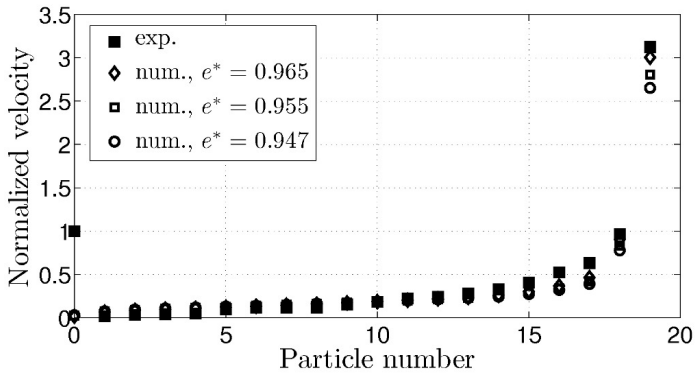

Figure 5: Normalized post-impact velocity of the balls obtained in the experimental test and in the numerical simulations with different values for the restitution coefficient.

We present in figure 6 the post-impact velocity, momentum and kinetic energy of the balls plotted in the semilog scale obtained from the experimental test and from the numerical simulation with $e_s = 0.965$ (which gives the best result of the post-impact velocity of the balls). In this figure, the overestimation of the post-impact velocity of the first balls by the model of multiple impact can be clearly observed. This overestimation leads to an overestimation of the post-impact momentum and kinetic energy of the balls. It can be noted that the mass of the balls considered in the numerical simulations might not match that in the experimental test. This might be also a source of discrepancy between the numerical and experimental result.

4.3 Conclusions

The numerical results in figures 5 and 6 cleary show that the LZB-complementarity multiple impact model supersedes the binary collision model employed in [19], see figure 6 in that paper. In figure 6 one sees that the post-impact velocities are not well predicted for the first 4 balls (like in figure 6.b in [19]), despite this comment should be mitigated in view of figure 5 which shows that the deviation is large only for the first ball. However for all the other balls the prediction is very good (for the last two balls the experimental and numerical results are too close to be distinguishable).

5 Simulations of the experimental tests in [18]

5.1 Description of the experimental tests

The configuration of the experimental tests performed by Melo *et al.* [18] is illustrated in figure 7. A monodisperse chain composed of 16 beads of diameter $\Phi_o = 26$ mm is placed in front of a tapered chain. Two tapered chains are

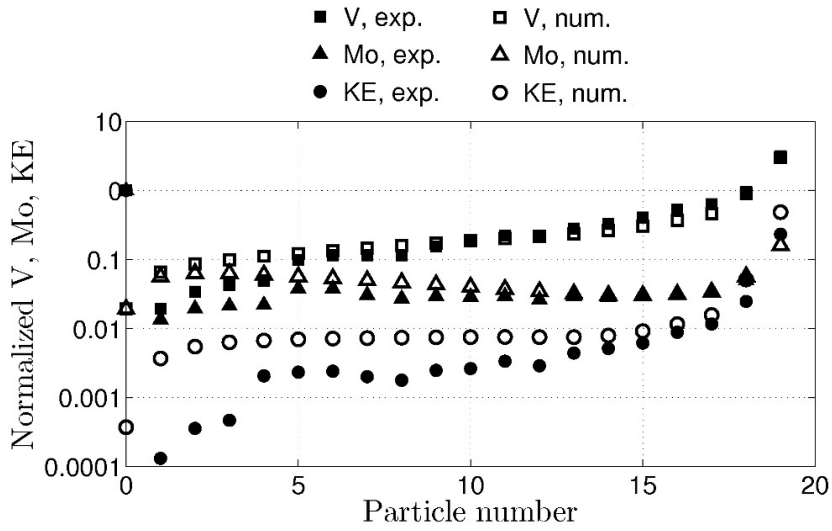

Figure 6: Normalized post-impact velocity, momentum and kinetic energy of the balls obtained in the experimental test and in the numerical simulations with different values for the restitution coefficient in the semilog scale.

considered: the first chain is composed of 14 beads with the tapering factor $q_1 = 5.6\%$ and the second one is composed of 12 beads with $q_2 = 8.27\%$. Beads are high carbon hardened steel whose properties are as follows: mass density $\rho = 7780\text{kg/m}^3$, Young modulus $E = 203$ GPa, Poisson ratio $\nu = 0.3$. The impactor is a smaller bead of diameter $\Phi_s = 8$ mm.

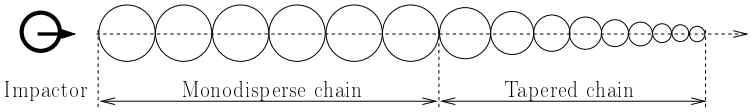

Figure 7: Configuration of the experimental test performed by Melo *et al. [18].*

During the experimental tests, the force at a given contact in the monodisperse chain is directly mesured by a sensor that is inserted in one of two adjacent beads at the contact. The force at a given contact in a tapered chain, for example the right contact of kth bead in the tapered chain, is indirectly measured as follows. First, the force at the end of a tapered sub-chain composed of 1, ..., k tapered beads, preceded by the monodisperse chain, is measured by a sensor made of the same material as the beads and placed at the end of the tapered sub-chain. The measured force can be represented as:

$$F^{wall} = F_m^{wall} \psi^{wall}\Big(\frac{t - T^{wall}}{\tau^{wall}}\Big), \tag{36}$$

where F_m^{wall} is the maximum force, ψ^{wall} is a function satisfying $0 \leq \psi^{wall} \leq 1$, T^{wall} is the time of flight and τ^{wall} is the pulse duration. Similarly, the force at

the right contact of the kth bead in the whole tapered chain can be represented as:

$$F^{chain} = F_m^{chain}\psi^{chain}\Big(\frac{t - T^{chain}}{\tau^{chain}}\Big). \tag{37}$$

From numerical simulations performed on a monodisperse chain composed of *perfectly elastic beads* followed by a rigid wall made of the same material as the beads (this wall is considered as the sensor wall used in the experimental tests), Job *et al.* [14] have found the following relations:

$$F_m^{wall} \approx 1.94 \times F_m^{chain}, \tau^{wall} \approx 1.09 \times \tau^{chain}. \tag{38}$$

Consequently, the force at the right contact of the kth bead in the whole tapered chain is obtained by scaling the force pulse measured at the end of the corresponding tapered sub-chain as follows:

$$F^{chain} = \frac{F_m^{wall}}{1.94}\psi^{wall}\Big(\frac{1.09(t - T^{chain})}{\tau^{wall}}\Big). \tag{39}$$

It is implicitly assumed in the scaling relation (39) that the shape of the force pulse at the right contact of the kth bead in the whole tapered chain is identical to that of the force pulse measured at the end of the correponding tapered sub-chain. The only difference between the force pulse at a contact in the whole tapered chain and at the end of the corresponding tapered sub-chain is the maximum force and the duration.

In order to check the accuracy of the scaling relation shown in (38), first we perform a numerical simulation on a monodisperse chain composed of 20 beads without contact with a rigid wall and compute directly the force pulse at the right contact of the 10th bead. Then we perform another numerical simulation on the monodisperse sub-chain that corresponds to the right contact of the 10th bead (this sub-chain is composed of 10 beads) followed a rigid wall made of the same material as the beads, and compute the force pulse at the rigid wall. A shock is induced at one end of each chain by a smaller bead. Two values of the restitution coefficient e_s are used: $e_s = 1.0$ for perfectly elastic collisions and $e_s = 0.965$ for non perfectly elastic collions ($e_s = 0.965$ is the value of the restitution coefficient obtained for the beads used in the experimental tests presented above by a fitting procedure that will be described in section 5.2). We are interested in the relation between the force pulses computed directly at the right contact of the 10th bead (contact between the 10th bead- the 11th bead) in the first simulation and at the end of the sub-chain (contact between the 10th bead and the wall) in the second simulation. The results obtained from the numerical simulations are as follows:

- for $e_s = 1.0$ we have $F_m^{wall} \approx 1.94 \times F_m^{chain}$, $\tau^{wall} \approx 1.09 \times \tau^{chain}$, and $T^{wall} \approx 1.02 \times T^{chain}$;
- for $e_s = 0.965$ we have $F_m^{wall} \approx 1.93 \times F_m^{chain}$, $\tau^{wall} \approx 1.09 \times \tau^{chain}$, and $T^{wall} \approx 1.02 \times T^{chain}$.

Furthermore, the shape of the force pulse at the contact in the chain is quite identical to that at the contact bead-wall for the two values of the restitution coefficient, see figure 8. Thus, the scaling relation presented in (39) seems to be good for a monodisperse chain composed of perfectly elastic beads or

inelastic beads with a small dissipation. However, in the case of a tapered chain composed of possibly non perfectly elastic beads, such a scaling relation might lead to erroneous results because the pulse tail is perturbed with oscillations by the rigid wall. This point will be analyzed later in this paper.

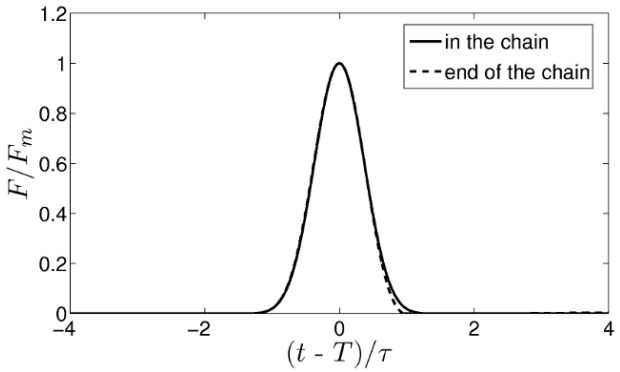

(a) $e_s = 1.0$

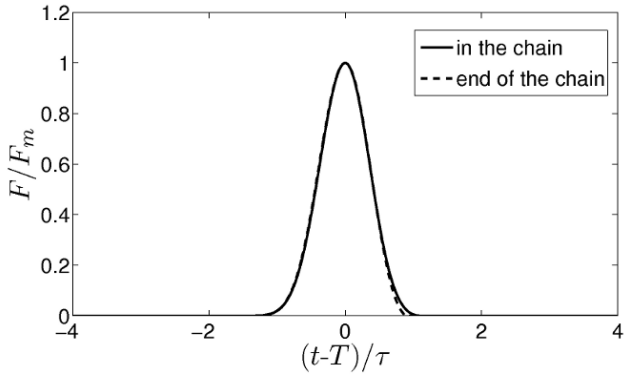

(b) $e_s = 0.965$

Figure 8: Normalized forces pulse computed at the right contact of 10th bead in a monodisperse chain of 20 beads and at the end of a monodisperse chain of 10 beads in contact with a rigid wall made of the same material than the beads: (a) for the restitution coefficient $e_s = 1.0$ and (b) for $e_s = 0.965$.

5.2 Fitting of parameters needed in numerical simulations

In order to perform numerical simulations of the experimental tests described above, in addition to the parameters given above, two other important parameters are necessary: coefficient of restitution and impact velocity of the the impactor, which are not given in [18]. It is thus necessary to determine these two parameters by a fitting procedure. The experimental data used for the fitting procedure is the maximum contact force along the monodisperse chain, which is extracted from figure 5 in [18]. It is worth noting that this experimental data is obtained by a direct measurement at the contacts in the monodisperse

chain without any extrapolation (the force at a given contact in the monodisperse chain is recorded by a sensor inserted in the left bead at the considered contact). We carry out numerical tests with different values of the coefficient of restitution, e_s, and of the impact velocity, V_{in}, on the monodisperse chain followed by the first tapered chain (14 beads with $q_1 = 5.6\%$). The fitting procedure illustrated in figure 9 consists in:

- first varying the value of the restitution coefficient, e_s, from 1 to 0 so that the decreasing tendency of the maximum force with the distance of the contacts can be the best matched;
- then varying the value of the impact velocity V_{in} so that the experimetal data can be quantitatively the best matched.

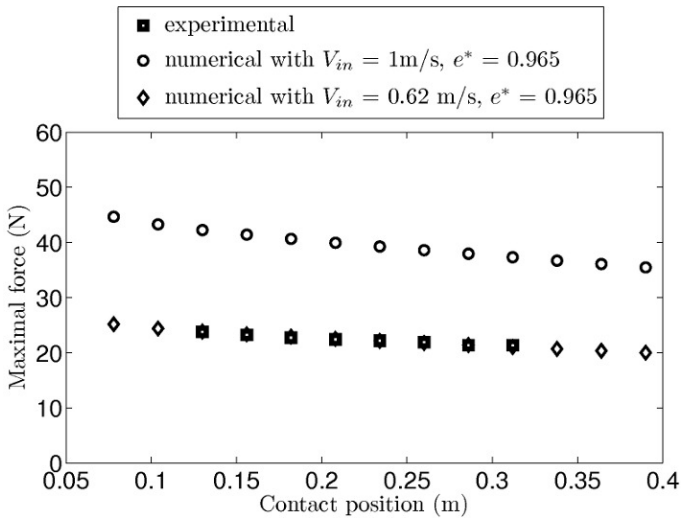

Figure 9: Fitting of the coefficient of restitution e_s and of the impact velocity V_{in} from the experimental data of the variation of the maximum force with the distance of the contacts in the monodisperse chain.

As shown in figure 9, with $e_s = 0.965$ and $V_{in} = 0.62\ m/s$ the numerical result fits well to the experimental data. Hereafter, we carry out numerical simulations on the considered tapered chains with these values.

5.3 Numerical tests

Two granular configurations are considered in the numerical simulations. The first one is composed of a monodisperse chain of 16 beads of diameter $\Phi_o = 26$ mm, followed by a tapered chain of 14 beads with a tapering factor $q_1 = 5.6\%$. For the second one, we replace the tapered chain in the first one by a tapered chain of 12 beads with $q_2 = 8.27\%$. In order to investigate the force pulses at the contact points in these tapered chains, we perform two types of numerical tests:

- Type 1: The numerical tests of this type are performed on the whole monodisperse chain, followed by tapered sub-chains with the number of beads varying from $n_1 = 0$ to $n_1 = 14$ for $q_1 = 5.6\%$, and from $n_2 = 0$ to $n_2 = 12$ for $q_2 = 8.27\%$. A rigid wall made of the same material as the beads is placed in contact with last beads in the tapered sub-chains. This type of tests is illustrated in figure 10.

- Type 2: The numerical tests of this type are performed on the whole monodisperse chain, followed by either the whole first tapered chain (14 beads with $q_1 = 5.6\%$) or the whole second tapered chain (12 beads with $q_2 = 8.27\%$). For this type of tests, there is no rigid wall at the end of the tapered chains. Figure 7 illustrates this type of tests.

With type 1 of numerical tests, we reproduce exactly what has been performed in the experimental process. The force pulse at a contact in the monodisperse chain is directly computed, whereas the force pulse at a contact in the tapered chain is extrapolated using the scaling relation (39). This kind of tests allows a direct comparison between the numerical and the experimental results. In the following, this method is referred to as "extrapolation method". Type 2 of numerical tests is complementary to type 1, for which the force pulse at a contact in the tapered chain is directly computed. In the following, this method is referred to as "direct computation method". Thanks to this type of numerical tests, we can evaluate the accuracy of the technique of measuring the force pulse at the contacts in a tapered chain carried out in [18].

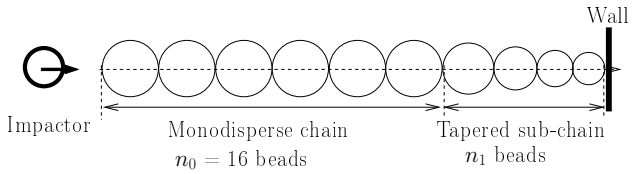

Figure 10: Numerical impact test on the monodisperse chain composed of 16 beads followed by a tapered sub-chain composed of n_1 beads placed in contact with a rigid wall.

We perform numerical simulations by using the LZB-complementarity multiple impact model. The interaction at contacts between two beads is modeled by the compliant bi-stiffness contact model with the elasticity coefficient $\eta = 3/2$. Parameters used in the numerical simulations are those given in [18] and by the fitting procedure: mass density $\rho = 7780\text{kg/m}^3$, Young modulus $E = 203$ GPa, Poisson ratio $\nu = 0.3$, coefficient of restitution $e_s = 0.965$, impact velocity $V_{in} = 0.62\ m/s$. The step size $\Delta P = 5 \times 10^{-7}\ N.s$ is used to perform the numerical simulations.

5.4 Comparison between numerical and experimental results

5.4.1 Force pulses felt at the rigid wall

In figure 11 (figure 12, respectively) we compare the force pulses computed at the rigid wall in the numerical tests of type 1 for different tapered sub-chains of n_1 beads with $q_1 = 5.6\%$ (n_2 beads with $q_2 = 8.27\%$, respectively) to the force pulses recorded at the rigid wall in the corresponding experimental tests. Figure 13 shows an overlap of all the force pulses shown in figures 11 and 12 by normalizing each force pulse by its peak and considering the time scale $(t-T)/\tau$ where T is the time of flight and τ is the pulse duration.

Some comments arise from figures 11, 12 and 13:

- The behaviour is well predicted qualitatively and quantitatively: the force pulse peak decreases when the length of the tapered sub-chains (n_1 or n_2) increases. The peak magnitude of the numerical force pulses is quite close to that of the experimental pulses.
- The tail of the force pulses increases and oscillates more when the length of the tapered sub-chains increases and when the tapering factor increases.
- In figure 12 one sees that the tail oscillations for $n_2 \geq 8$ are very well predicted.
- The pulse shape is too sharp (it has a too narrow base) in the simulations, *i.e.* the beginning of the tail is not perfectly reproduced numerically. This is visible also in figure 13.
- It is noteworthy that the front of the pulse remains almost unchanged when n_1 or n_2 is increased. This suggests that in case of the tapered chain, the pulse consists of the monodisperse pulse (a soliton) with a perturbation at the tail. This might be due to the presence of the rigid wall at the end of the tapered sub-chains, that leads to a reflection of the wave when it reachs this rigid wall.

5.4.2 Maximum forces at contacts

As presented in section 5.1, in the experimental tests the force pulses at the contacts in the considered tapered chains are not directly recorded. They are obtained by the extrapolation method with the scaling relation (39). The maximum force at a given contact in the tapered chains (F_m^{chain}) presented in figure 5 of [18] is thus the maximum force at the rigid wall measured in the test with the corresponding tapered sub-chain (F_m^{wall}) divided by a reduction factor equal to 1.94. For instance, the maximum force at the right contact of the n_1th bead in an entire tapered chain (tapering factor q) ($F_m^{chain}(n_1)$) is computed as $F_m^{chain}(n_1) = F_m^{wall}(n_1)/1.94$ with $F_m^{wall}(n_1)$ being the maximum force measured at the rigid wall in the test with the corresponding tapered sub-chain of n_1 beads with the same tapering factor q.

In the numerical tests the maximum force at a given contact in the tapered chain can be either computed indirectly by the same extrapolation method as in the experimental tests with the scaling relation (39), or computed directly at

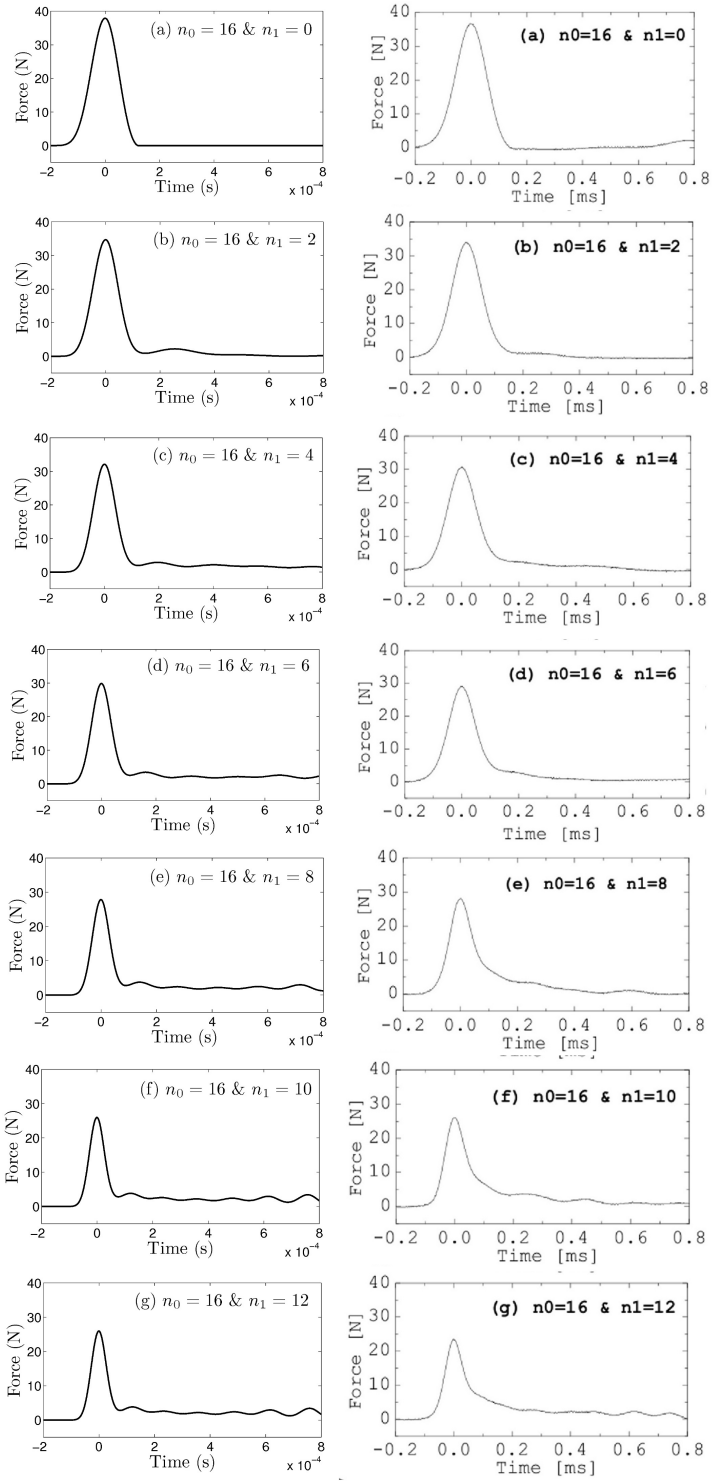

Figure 11: Force pulses computed at the rigid wall during the numerical tests of type 1 for different tapered sub-chains with $n_1 = 0$, 2, 4, 6, 8, 10, 12 (left column) compared to force pulses measured directly at the rigid wall in the experimental tests [18] (right column) for $q_1 = 5.6\%$.

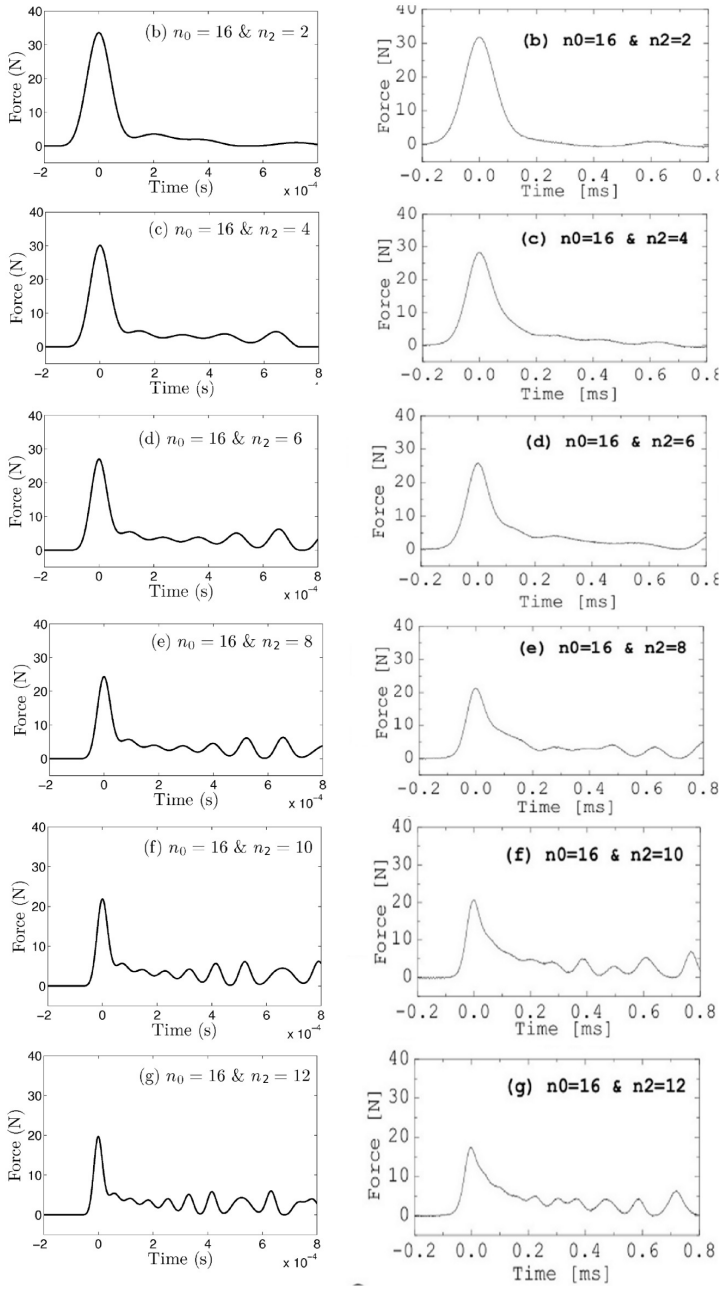

Figure 12: Force pulses at the rigid wall during the numerical tests of type 1 for different tapered sub-chains with $n_1 = 0,\ 2,\ 4,\ 6,\ 8,\ 10,\ 12$ (left column) and force pulses measured directly at the rigid wall in the experimental test [18] (right column) for $q_2 = 8.27\%$.

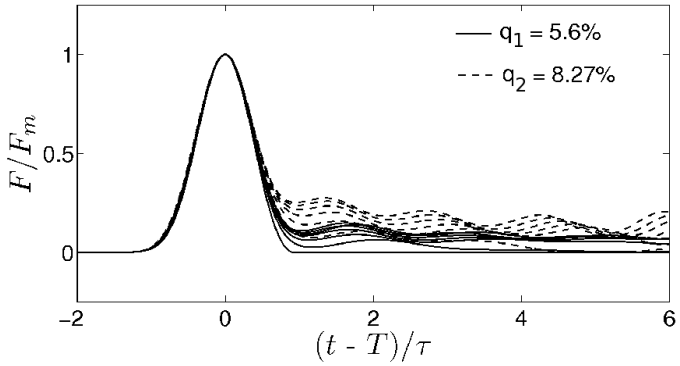

(a) Numerical

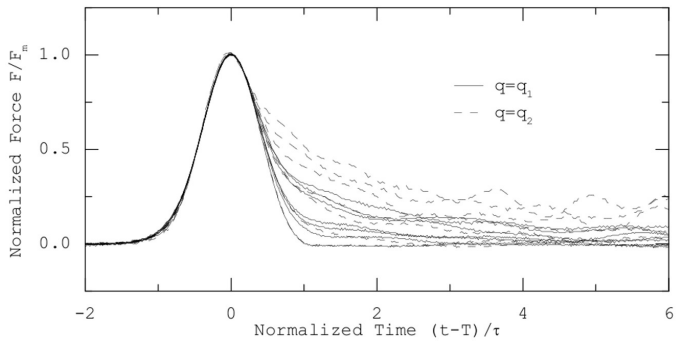

(b) Experimental

Figure 13: Collapse of the pulses presented in figures 11 and 12 when the force is normalized to the maximum force, F_m, and the time scale is $(t-T)/\tau$ where T and τ are the measured time of flight and pulse duration, respectively. (a) for the numerical data and (b) for the experimental data.

the considered contact in the numerical test of type 2. The numerical results corresponding to the two types of tests are compared to the experimental results as shown in figure 14 for the two considered tapered chains with $q_1 = 5.6\%$ (subfigure 14a) and $q_2 = 8.27\%$ (subfigure 14b).

As shown in figure 14, the maximum forces at the contacts in the tapered chains obtained from the numerical simulations are quite close to the experimental results for both extrapolation method and direct computation method. However, it can be observed that the extrapolation method leads to a slight overestimation of the maximum forces computed directly at the contacts in the tapered chains. This discrepancy can be attributed to the reduction factor of 1.94 used in the scaling relation (39). In fact, as analysed in section 5.1, this value is determined through numerical simulations performed on non-dissipative monodisperse chains. Considering the same value for tapered chains is not relevant because dynamics of tapered chains is very different from dynamics of monodisperse chains. We might use the same reduction factor for all the contacts in a monodisperse chain because the couple of beads in contact is the same for all the contacts. However, for a tapered chain for which the size of the

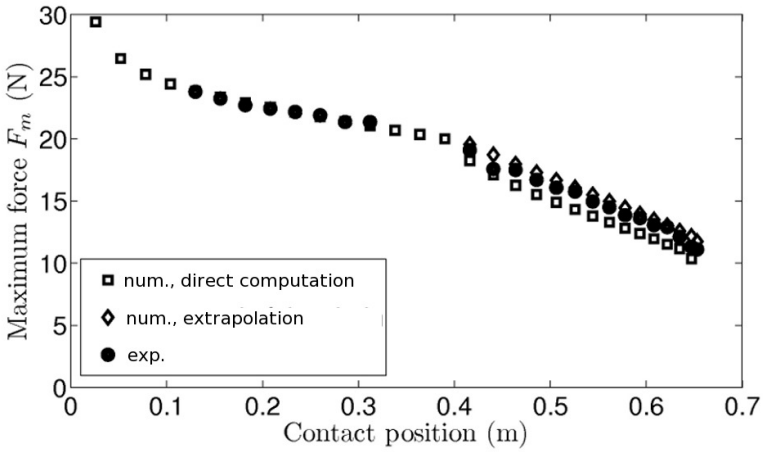

(a) $q_1 = 5.6\%$

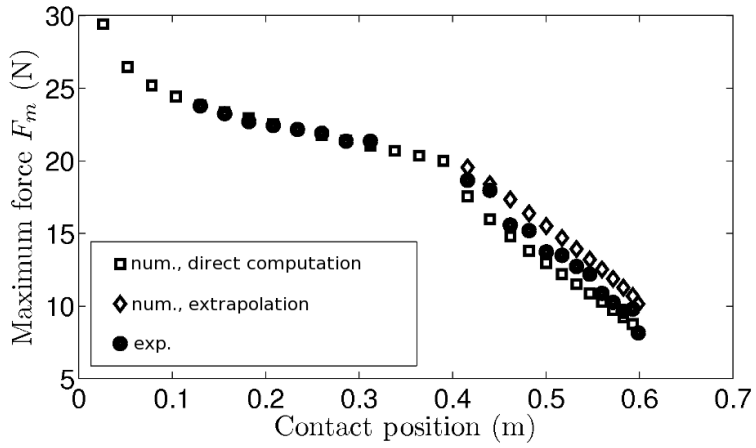

(b) $q_2 = 8.27\%$

Figure 14: Maximum force versus the contact position obtained from the numerical simulations of the two types of tests, compared to the experimental results. (a) for $q_1 = 5.6\%$ and (b) for $q_2 = 8.27\%$. The symbols $\diamond$ and $\square$ represent respectively the maximum force at the contacts in the tapered chains obtained with the extrapolation method with the scaling relation (38) from the maximun force at the rigid wall computed in the numerical tests of type 1, and with the direct computation at these contacs in the numerical tests of type 2. The symbol $\bullet$ represents the experimental results.

beads is increased, the couple of beads in contact is different from one contact to another. As a result, the reduction factor might not be the same for all the contacts in the tapered chain and might depend on the tapering factor q.

5.4.3 Duration of the force pulse at contacts

The pulse duration τ is determined by fitting the Nesterenko solution

$$F(t) = F_m cos^6\Big(\frac{t-T}{\tau}\Big), \tag{40}$$

to the experimental data for the pulse front. This method is used in [18]. Similarly to the maximum contact force, the duration of the force pulse at a given contact in a tapered chain is experimentally extrapolated from that of the force pulse measured at the rigid wall sensor, according the scaling relation $\tau^{chain}(n_1) = \tau^{wall}(n_1)/1.09$. Here $\tau^{wall}(n_1)$ is the duration of the force pulse measured at the rigid wall sensor in the test with a tapered sub-chain composed of n_1 beads with the same tapering factor q.

In the numerical tests the duration of the force pulse at a given contact in a tapered chain can be either computed indirectly by the same extrapolation method as in the experimental tests, or computed directly at the considered contact in the numerical test of type 2. The numerical results corresponding to the two types of tests are compared to the experimental results as shown in figure 15 for the two considered tapered chains with $q_1 = 5.6\%$ (subfigure 15a) and $q_2 = 8.27\%$ (subfigure 15b).

As shown in 15, the numerical results obtained with both extrapolation method and direct computation method match well the experimental results. The numerical simulations overestimate slightly the pulse durations obtained in the experimental tests. We can note a slight discrepancy between the pulse duration obtained with the extrapolation method and that obtained from the direct computation method. This discrepancy might be due to the same reasons as those analyzed in section 5.4.2. However, the discrepancy between these two methods in terms of pulse duration is less significant than in terms of maximum force.

5.4.4 Wave speed

The speed of the wave when it passes through a given bead i is computed as:

$$v_i = \frac{\Phi_i}{T_i - T_{i-1}}, \tag{41}$$

where T_{i-1} and T_i are, respectively, the time of flight at the left and right contact of bead i whose diameter is Φ_i. Experimentally, the time of flight at a contact in the monodisperse chain is directly measured by the sensor inserted in the left bead at the considered contact and the time of flight at a contact in a tapered chain is measured by the sensor at the rigid wall in the test with the corresponding tapered sub-chain. Numerically, the time of flight of the force pulse at a given contact in a tapered chain can be either computed at the rigid wall in the corresponding test of type 1 or computed directly at the considered contact in the the test of type 2. The numerical results corresponding to the two types of tests are compared to the experimental results as shown in figure 16 for the two considered tapered chains with $q_1 = 5.6\%$ (subfigure 16a) and $q_2 = 8.27\%$ (subfigure 16b).

We can see in figure 16 the wave speed obtained numerically with the time of flight computed at the rigid wall in the numerical tests of type 1 (extrapolation

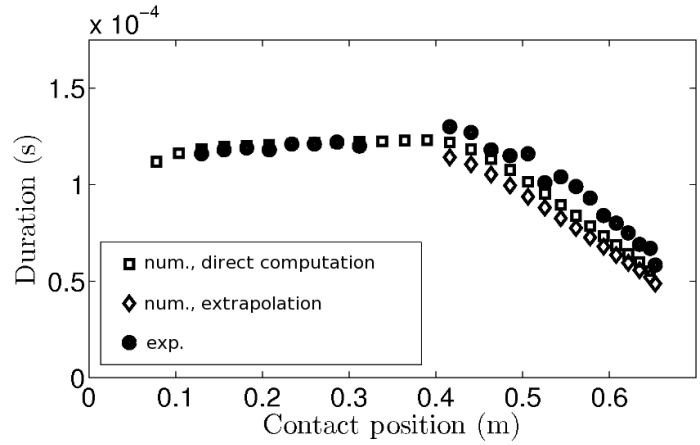

(a) $q_1 = 5.6\%$

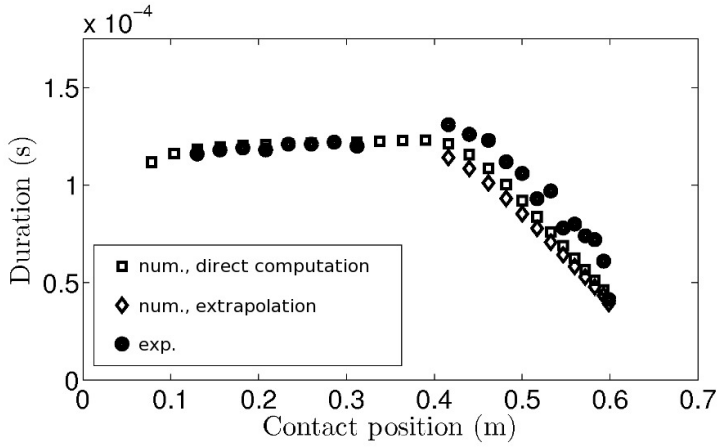

(b) $q_2 = 8.27\%$

Figure 15: Duration of the force pulse versus the contact position obtained from the numerical simulations of the two types of test, compared to the experimental results. (a) for $q_1 = 5.6\%$ and (b) for $q_2 = 8.27\%$. The symbols $\diamond$ and $\square$ represent, respectively, the duration computed indirectly by the scaling relation (38) from the duration computed at the rigid wall in the numerical tests of type 1, and the duration computed directly at the contact in the chains in the numerical tests of type 2. The symbol $\bullet$ represents the experimental results.

method) is very close to that obtained with the time of flight computed directly at the contacts in the tapered chains in the numerical tests of type 2. This is not surprising since the time of flight T^{chain} for a pulse to reach a given contact in a tapered chain is very close to the time of flight T^{wall} for the same pulse to reach the rigid wall that is placed at the end of the corresponding tapered sub-chain. As shown in section 5.1, for monodisperse chains $T^{wall} \approx 1.02 \times T^{chain}$. Indeed, to reach a given contact in the tapered chains, the waves in both types of nu-

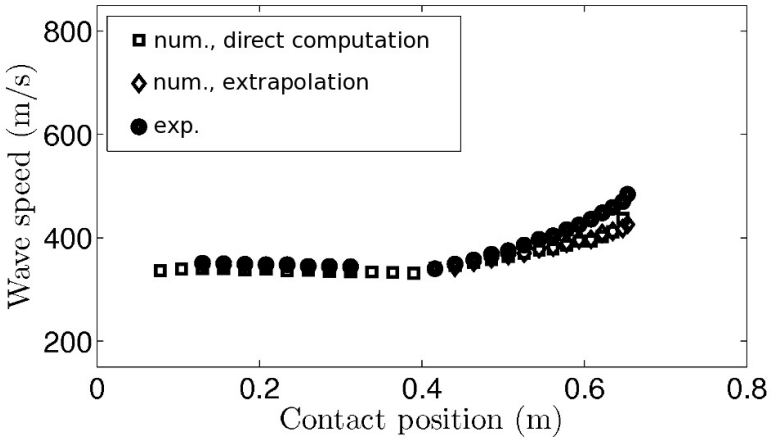

(a) $q_1 = 5.6\%$

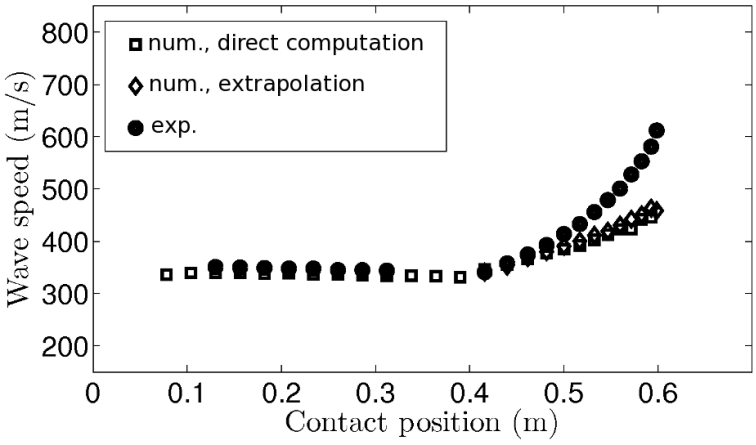

(b) $q_2 = 8.27\%$

Figure 16: Wave speed versus the contact position obtained from the numerical simulations of the two types of tests, compared to the experimental results. (a) for $q_1 = 5.6\%$ and (b) for $q_2 = 8.27\%$. The symbols $\diamond$ and $\square$ represent, respectively, the wave speed computed from the time of flight of the force pulse at the rigid wall for the numerical tests of type 1, and from the time of flight at the contact in the chains for the numerical tests of type 2. The symbol $\bullet$ represents the experimental results.

merical tests have to travel on the same monodisperse chain and than on the same tapered sub-chain corresponding to the considered contact. It can be observed that the numerical simulations can predict qualitatively the acceleration of the wave when travelling in the tapered chains. Nevertheless, the discrepancy between the wave speed obtained from the numerical simulations and the wave speed measured in the experimental tests is significant for the tapered chain with $q_2 = 8.27\%$. It is worth noting that the experimental data on the wave

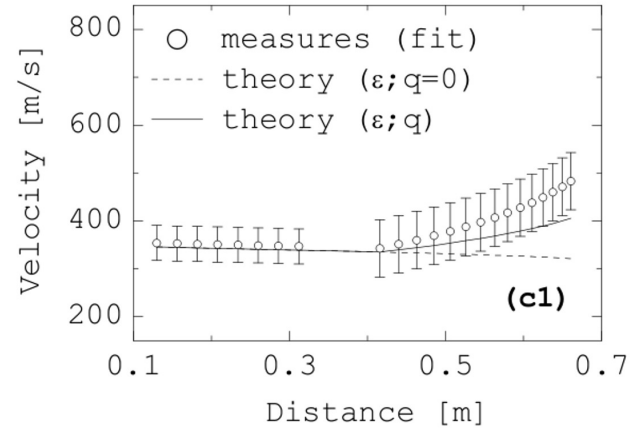

(a) $q_1 = 5.6\%$

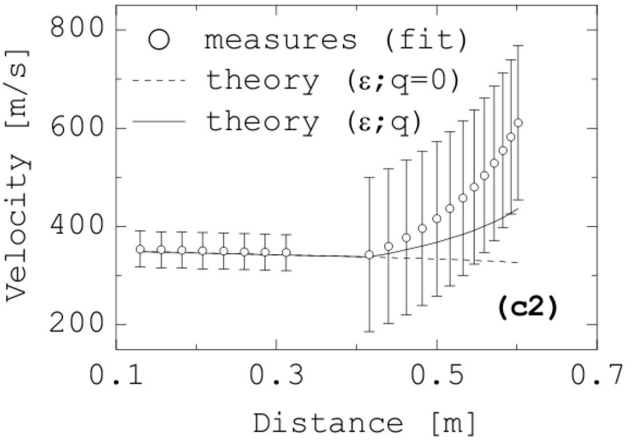

(b) $q_2 = 8.27\%$

Figure 17: Experimental data on the wave speed presented in [18]. (a) for $q_1 = 5.6\%$ and (b) for $q_2 = 8.27\%$.

speed presented in [18] is not reliable, due to a very large relative errors when estimating the wave speed from the time of flight difference, as shown in figure 17. In order to capture the central tendency from the experimental data, the authors in [18] use a smoothing procedure. The smoothing procedure consists in fitting the relation $v_i = Qv_{i-1}$ with Q being a constant to the experimental data. The relation $v_i = Qv_{i-1}$ results from the so-called quasi-solitary wave approximation combined with binary collision model. The accuracy of such a relation is questionable. The experimental data that we show in figure 16 is the result of this smoothing procedure so the results should be considered at a qualitative level rather than a quantitative level concerning the wave speeds.

5.4.5 Impulses for the front and for the tail of the pulse

Impulses for the front (P_F) and for the tail (P_T) of a force pulse are defined as follows:

$$P_F = \int_{-\infty}^{T+\tau} F(t)dt, \tag{42}$$

$$P_T = \int_{T+\tau}^{+\infty} F(t)dt. \tag{43}$$

In the case that the force pulse at a contact in the tapered chains is extrapolated with the scaling relation (39), the impulses P_F and P_T for the considered contact are computed as follows:

$$\begin{aligned} P_F^{chain} &= \int_{-\infty}^{T^{chain}+\tau^{chain}} F^{chain}(t)dt = \frac{1}{1.09\times 1.94}\int_{-\infty}^{T^{wall}+\tau^{wall}} F^{wall}(t)dt \\ &= \frac{1}{1.09\times 1.94}P_F^{wall}, \end{aligned} \tag{44}$$

$$\begin{aligned} P_T^{chain} &= \int_{T^{chain}+\tau^{chain}}^{\infty} F^{chain}(t)dt = \frac{1}{1.09\times 1.94}\int_{T^{wall}+\tau^{wall}}^{\infty} F^{wall}(t)dt \\ &= \frac{1}{1.09\times 1.94}P_T^{wall}. \end{aligned} \tag{45}$$

Let us first compare the front impulse P_F and the tail impulse P_T obtained by the extrapolation method described above in the numerical tests of type 1 and in the experimental tests. From a qualitative point of view, the numerical simulations predict rather well the evolution of the front and tail impulses at the contacts in the monodisperse and tapered chains, as shown in figure 18. However, there is a discrepancy between the numerical and experimental results: the numerical simulations underestimate the front impulse P_F and overestimate the tail impulse P_T. This discrepancy can be also observed for the contacts in the monodisperse chain for which the maximum contact force and the duration of the force pulse fit rather well to the experimental ones (see figures 14 and 15), which is likely due to the difference between the numerical pulse shape and the experimental one. This discrepancy becomes more significant at the contacts in the tapered chains (contact positions ≥ 0.45 m), which is essentially due to the discrepancies in terms of maximum force and pulse duration obtained with the extrapolation method in the numerical tests of type 1 and in the experimental tests. Practically, the force pulse is recorded in the experimental tests using a high frequency measurement with a fixed set of points. This technique allows the pulse front to be fully recorded (high precision) but not the pulse tail (the very end of pulse tail is not recorded). Consequently, it is difficult to compare the tail impulse P_T for the experimental pulses that are not fully recorded to the tail impulse P_T for the numerical pulses that are fully computed in the numerical tests of type 1.

Now we compare the front impulse P_F and the tail impulse P_T at the contacts in the tapered chains obtained with the extrapolation method in the numerical tests of type 1 to those obtained with the direct computation method in the

numerical tests of type 2. We recall that for the direct computation method, first we compute directly the force pulses at the contacts in the tapered chains during the numerical tests of type 2, and then we integrate these force pulses to obtain the front and tail impulses, as shown in equations (42) and (43). As can be seen in figure 18, the front impulses P_F obtained with both methods are quite close whereas the tail impulses P_T are very different. The tail impulse P_T obtained with the direct computation method is very small with respect that obtained with the extrapolation method. This result shows that the tail of the pulse at a contact in a tapered chain obtained by extrapolating the pulse computed at the rigid wall in the numerical tests of type 1 is much more pronounced than that obtained by computing directly at the considered contact in the numerical tests of type 2. We will analyze this point in the next section.

5.4.6 Force pulses obtained from the direct computation

We analyze numerically whether or not the experimental measurement technique described in section 5.1 allows to capture the force pulse propagating in a tapered chain. We recall that the force pulse at a contact in a tapered chain is experimentally measured by extrapolating using the scaling relation (39). For this objective we will compare the force pulses at the contacts in the considered tapered chains obtained by the extrapolation method and by the direct computation method. As shown in figure 14, the extrapolation method leads to a slight overestimation of the maximum force computed directly at the contacts. In terms of duration and of speed of the pulse, the extrapolation gives results that are close to those computed directly at the contacts in the tapered chains, as shown in figures 15 and 16. In figure 19, we compare the shape of the force pulses obtained by the extrapolation method in the numerical tests of type 1 (a rigid wall is placed at the end of tapered sub-chains) and by the direct computation method in the numerical tests of type 2 (the whole tapered chains are considered without rigid wall at the their end). As can be seen in this figure, the fronts of the force pulses obtained by the extrapolation method are similar to those obtained from the direct computation method. However, the tail of the force pulses obtained by the extrapolation method is much more pronounced than that obtained by the direct computation method. It can be also noted that for the force pulses obtained from the direct computation method, their tail is very small compared to their front. This is the reason why when the force pulses computed directly at the contacts in the tapered chains, the tail impulse P_T is negligeable with respect to the front impulse P_F as shown in figure 18. In fact, in the numerical tests of type 2 for which no rigid wall is placed at the end of the tapered chains, a pulse initiated at the largest end of the tapered chains propagates down the chains and comes out of the chains without reflection. Consequently, the force pulse at a given contact in the tapered chains corresponds to a coming-in and a coming-out of the wave when it passes through the considered contact (a compression phase followed by an expansion phase). In the numerical tests of type 1 for which a rigid wall is placed after tapered sub-chains, the pulse will hit the rigid wall and then will reflect. The pulse after reflection propagates in the direction of an increasing bead diameter (we can consider this case as a pulse propagating in an anti-tapered chain). For such a configuration, part of pulse propagates toward the largest end and part is reflected once again toward the rigid wall. Consequently, the force pulse

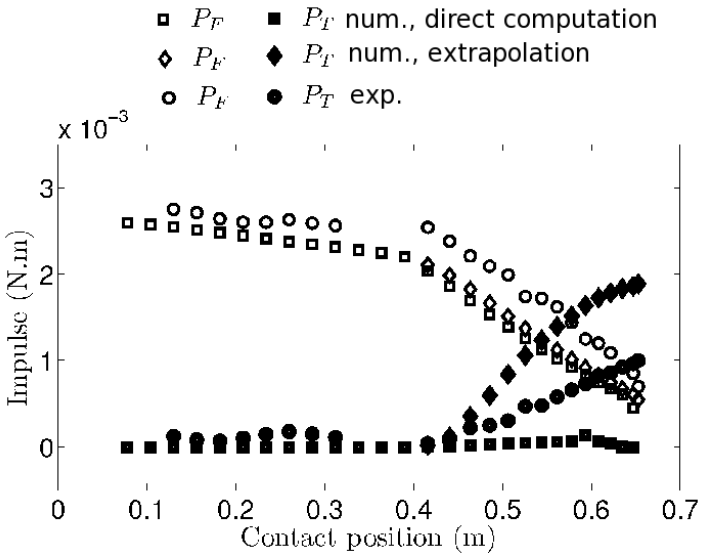

(a) $q_1 = 5.6\%$

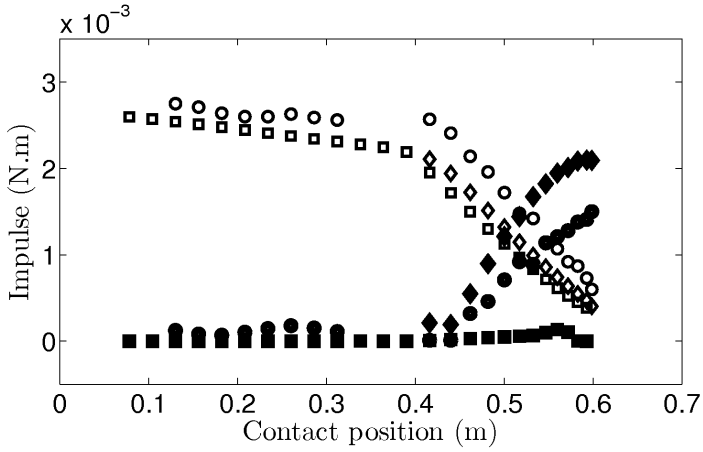

(b) $q_2 = 8.27\%$

Figure 18: Impulses for the front (P_F) and for the tail (P_T) of the pulse versus the contact position obtained from the numerical simulations of the two types of test, compared to the experimental result. (a) for $q_1 = 5.6\%$ and (b) for $q_2 = 8.27\%$. The symbols $\diamond$ and $\square$ represent, respectively, the wave speed computed from the time of flight of the force pulse at the rigid wall for the numerical tests of type 1, and from the time of flight at the contact in the chains for the numerical tests of type 2. The symbol $\circ$ represents the experimental results. (a) for $q_1 = 5.6\%$ and (b) for $q_2 = 8.27\%$.

computed at the end of the rigid wall corresponds to various coming-in and reflection travels (multiple compression and expansion phases which can be taken into account with the LZB-complementarity multiple impact model). The well

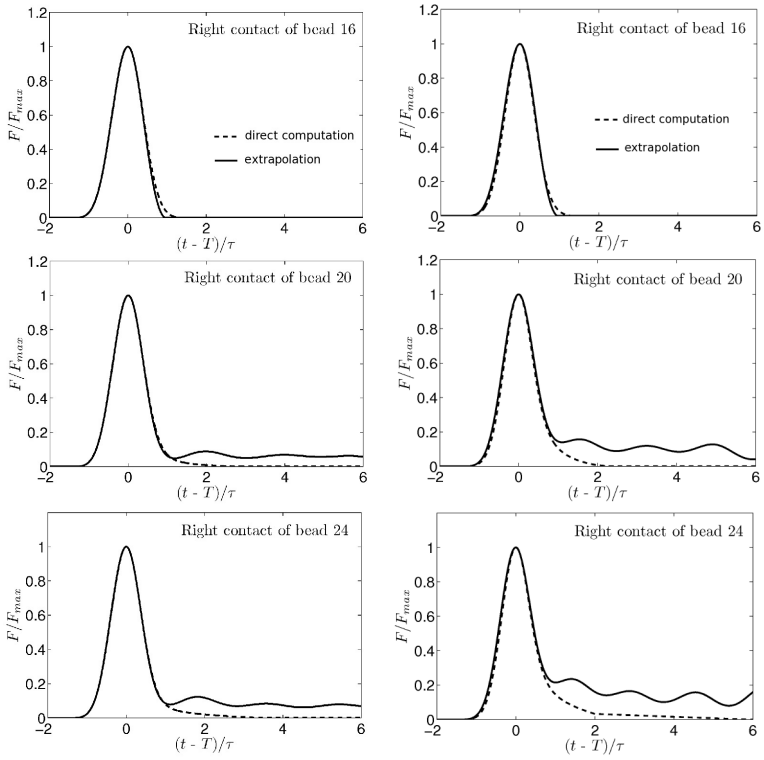

(a) $q_1 = 5.6\%$ (b) $q_2 = 8.27\%$

Figure 19: Overlap of force pulses computed directly at contacts in tapered chains in the numerical tests of type 2 and extrapolated from force pulses at the end of the rigid wall in the numerical tests of type 1. Force is normalized by the maximum force and the time scale is $(t-T)/\tau$ (a) for $q_1 = 5.6\%$ and (b) for $q_2 = 8.27\%$.

pronounced tails of the force pulses in this case are certaintly due to this complex phenomenon. Therefore the force pulses computed directly at the contacts in the considered tapered chains in the numerical tests of type 2 and those extrapolated from the force pulses computed at the rigid wall in the numerical tests of type 1 do not result from the same physical phenomenon, in particular for the tails. These numerical results show that the well pronounced tails of the force pulses obtained in the experimental tests shown in [18], in particular the oscillations at the tails result, on one hand, from the mechanical effects of tapered chains and, on the other hand, from the presence of a rigid wall placed at the end of tapered sub-chains.

5.4.7 Conclusions

In sections 5.4.2, 5.4.3, 5.4.4, 5.4.5, 5.4.6, we compare the features of the force pulses propagating in two tapered chains with tapering ratio $q_1 = 5.6$ and $q_2 = 8.27\%$ such as the pulse shape, the amplitude, the pulse duration, the

propagation speed, the front and tail impulses obtained from the experimental tests presented in [18] and from the numerical simulations with the LZB-complementarity model. In the experimental tests, the force pulse at a contact in a given tapered chain is obtained by extrapolating the force pulse measured at a rigid wall that is placed at the end of the tapered sub-chain corresponding to the considered contact (extrapolation method). In the numerical simulations, we carried out the same tests as the experimental ones. We also carried out numerical tests on the whole considered tapered chain for which the force pulse at a contact in the tapered chain can be computed directly (direct computation method). In fact, the impact velocity and the resitution coefficient are not available in [18], so we determined these parameters by the fitting procedure. The fitting procedure is performed in order to match the experimental data available for the monodisperse chain presented in [18]. The obtained values for the impact velocity and the restitution cofficient are then used to simulate the considered tapered chains. Comparing the numerical results to the experimental ones and the numerical results obtained by the extrapolation method to those obtained by the direct computation method, the following conclusions can be drawn:

- The numerical simulations can reproduce rather well the features of force pulses (front, amptitude, duration, the tail, the oscillations at the tail, etc.) observed in the experimental tests. More precisely, the amptitude and the duration of force pulses are quantitatively well predicted.
- The wave speed measured experimentally is qualitatively well predicted by the numerical simulations. However, it is not suitable to compare quantitatively the wave speed obtained from the experimental tests to those obtained from the numerical simulations because the experimental technique of measuring the wave speed gives large errors.
- The front and tail impulses are qualitatively well predicted by the numerical simulations. Quantitatively the numerical simulations underestimate the front impulse and overestimate the tail impulse obtained from the experimental tests. The overestimation of the tail impulse by the numerical simulations might result from the fact that the tail of the force pulses is not fully recorded in the experimental tests whereas it is fully computed in the numerical simulations.
- The tail of the force pulses obtained numerically from the direct computation method is very small compared to that obtained from the extrapolation method. The well pronounced tail of the force pulses obtained from the extrapolation method in the numerical simulations and in the experimental tests might due to partly the presence of the rigid wall placed at the end of the tapered sub-chains. Therefore, it is likely that the measurement technique described in [18] is not suitable to investigate the force pulses that actually are exerted at the contacts in a free tapered chain.

6 Simulation of impact dynamics within stepped chains

In this section, we turn our attention to impact dynamics within stepped chains, which are composed of a monodisperse section of large beads followed by a

monodisperse section of small beads. A typical feature of these granular chains is that a solitary wave (SW) propagating in the large section turns into a solitary wave train (SWT), containing many signle solitary waves with decreasing amplitudes when it passes though the small section. Such a SWT has been first observed in the experimental tests presented in [27, 28] when a large enough striker impacts a small monodisperse chain. The formation of the SWT has been numerically confirmed in [31]. Job *et al.* have been carried a series of experimental tests on stepped chains and have put in evidence the formation of the SWTs within such granular chains. In the following, we present the numerical results obtained from the simulations of the tests in [31] performed with the LZB-complementarity multiple impact model.

6.1 Test configuration

The considered granular chains is composed of two sections: the first section contains 7 large beads of radius $R_1 = 13\ mm$ and the second section contains up to 50 small beads of radius $R_2 = 6.5\ mm$. The beads in the chain are initially stationary and barely touch each other. The chains are then impacted at one end by a striker of radius $R_s = 6.5\ mm$. The beads in the chains and the striker are made of high carbon chrome hardened steel with the following properties: Young modulus $E = 203\ GPa$, Poisson coefficient $\nu = 0.3$ and the mass density $\rho = 7780\ kg/m^3$. The wall is assumed to be made of the same material as the beads in the chains. Aside from the parameters given in [30], we need to know the restitution coefficient and the impact velocity in order to perform the numerical simulations. These parameters will be determined by a fitting procedure. Two ways are considered:

- in the first way, we assume that the constitutive material of the beads is purely elastic. This means that there is no energy dissipation during collisions ($e_s = 1.0$). In this case, we change the impact velocity in such a way that the maximum force of the incident wave (wave before the interface) obtained from the numerical simulations fits to the experimental results shown in figure 2.a in [30]. We obtain an impact velocity $V_{in} = 0.31\ m/s$.

- in the second way, we change both the restitution coefficient and the impact velocity such that the first peak of the solitary wave trains shown in figures 2.b and 2.c in [30] can be reproduced from the numerical simulation. In this case, we obtain $e_s = 0.98$ and $V_{in} = 0.40 m/s$. The value of the restitution coefficient obtained here is in accordance with the range of the restitution coefficient obtained experimentally for steel beads (around 0.95) and close to the value that we obtained from the fitting procedure presented in section 5 for beads made of the same material ($e_s = 0.965$).

In the sequel, we will present numerical results obtained with two couples of parameters ($e_s = 1.0$, $V_{in} = 0.31\ m/s$) and ($e_s = 0.98$, $V_{in} = 0.40\ m/s$) for the restitution coefficient and the impact velocity. The numerical simulations are performed with the bistiffness compliance contact model and the step size $\Delta P = 10^{-6}\ N.s$.

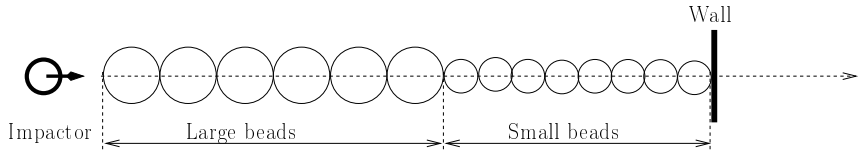

Figure 20: Numerical impact test on a stepped chain composed of two sections: large beads are in the first section and small beads are in the second section.

6.2 Numerical result with $e_s = 1.0$ and $V_{in} = 0.31\ m/s$

As can be seen in figure 21, the solitary wave train is well reproduced in the numerical simulations for the stepped chains. The times of flight for the SW and the SWTs to reach the wall and the times of flight of SWs in SWTs in the numerical simulations are in good accordance with the exprimental data. Moreover, the duration of each SW in the SWTs is close to the experimental duration. However, the number of significant SWs in the SWTs obtained from the numerical simulations is higher than that found in the experimental tests (about 7 in the numerical simulations and 5 in the experimental tests). This might be due to the effect of friction between the beads and the rail that is not taken into account in the numerical simulations. For the first SWT obtained with 25 small beads, the force amplitude of SWs fits very well to the experimental data (see figure 22a) but this is less good for the second SWT obtained with 50 small beads (see figure 22b). We can see that, in the experimental data the force amplitude of SWs in the second SWT is reduced in comparison with the first SWT. This is natural since the SWT has to travel a longer distance before reaching the wall and the SWT is attenuated by the dissipative mechanisms at the contact points. In the present simulations, this dissipation is not taken into account, this is the reason why the second SWT is quite similar to the first SWT. To better reproduce the second SWT, it is necessary to introduce the dissipation into the numerical simulation.

In figure 23, we compare the force pulse at the interface obtained from the numerical simulations to that obtained from the experimental tests. It can be seen that the numerical simulations give a result that is quite similar to the experimental one. The numerical force amplitude at the interface is lower than the experimental force amplitude. The ratio of the force amplitude at the interface to the incident force amplitude is equal to 0.36 in the experimental test whereas a value of 0.31 is found in the numerical simulations.

6.3 Numerical results with $e_s = 0.98$ and $V_{in} = 0.40\ m/s$

As shown in figure 24, when the dissipation is introduced into the numerical simulations by using the restitution coefficient $e^* = 0.98$, the SWT is attenuated when it travels in the chain (in figure 21 the peaks of the SWT remain constant while in figure 24 the peaks of the SWT decrease significantly). Figures 25 compares the force at the peaks in the first SWT (figure 25a) and in the second SWT (figure 25b) obtained from the numerical simulations and from the experimental tests. We can see that the numerical simulations with the local dissipation give a result that fits well to the experimental data except

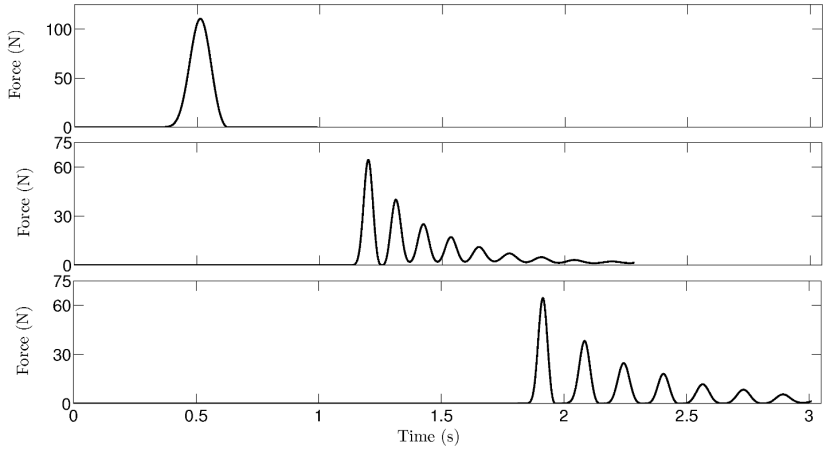

(a) numerical result

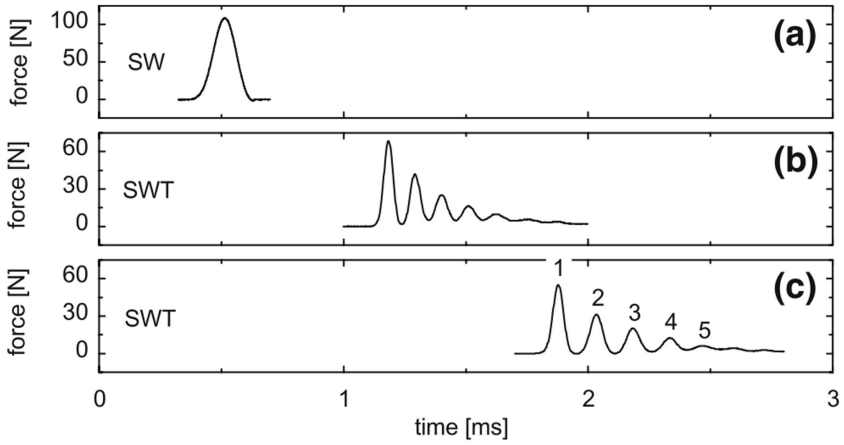

(b) experimental result

Figure 21: Solitary wave and solitary wave trains in stepped chains obtained from the numerical simulations (a) and from the experimental tests [30] (b). First row corresponds to the force recorded at the end of a monodisperse chain composed of 7 beads of radius $R_1 = 13\ mm$. Second (resp. last) row corresponds to the force recorded at the end of a stepped chain composed of 7 beads of radius $R_1 = 13\ mm$ and 25 (resp. 50) beads of radius $R_2 = 6.5\ mm$. The numerical simulations are performed with $e_s = 1.0$ and $V_{in} = 0.31\ m/s$.

some small peaks in the end of SWTs. However, introducing the local dissipation ($e_s = 0.98$) overestimates the incident force recorded before the interface (shown in the first row of figure 24).

The incident force and the force at the interface obtained from the numerical simulations with the couple of parameters ($e_s = 0.98$ and $V_{in} = 0.40\ m/s$) are shown in figure 26. The force amplitude at the interface obtained from the numerical simulations (23 N) is higher than the experimental data (20 N). In

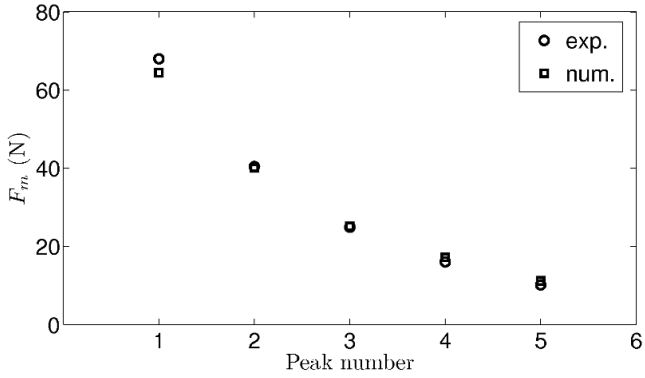

(a) with 25 beads of $R_2 = 6.5\ mm$

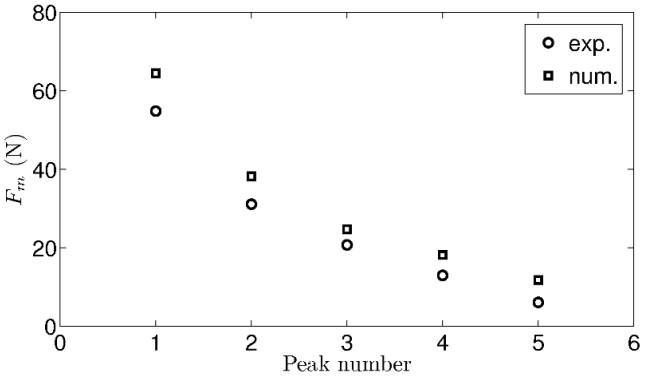

(b) with 50 beads of $R_2 = 6.5\ mm$

Figure 22: Force at the peaks in the solitary wave train obtained from the numerical simulations, compared to the experimental data for the solitary wave train at the end of the stepped chain with 25 beads of $R_2 = 6.5\ mm$ (a) and 50 beads of $R_2 = 6.5\ mm$ (b). The numerical simulations are performed with $e_s = 1.0$ and $V_{in} = 0.31\ m/s$.

the other hand, the ratio of the force amplitude at the interface to the incident force amplitude obtained from the numerical simulations (0.3) is lower than that obtained from the experimental tests.

6.4 Conclusions

In this section, we simulated impact dynamics of stepped chains. This kind of granular chains generate the solitary wave trains (SWTs) that are composed of a set of solitary waves with decreasing amplitude. The simulations are performed for two cases without or with local dissipation at contact points. As a whole, the numerical simulations reproduce rather well the SWTs observed in the experimental tests presented in [30]. The times of flight of the SWTs and of SWs in SWTs are in good accordance with the experimental data. In the case without local dissipation, the peaks of first SWTs shown in [30] are well

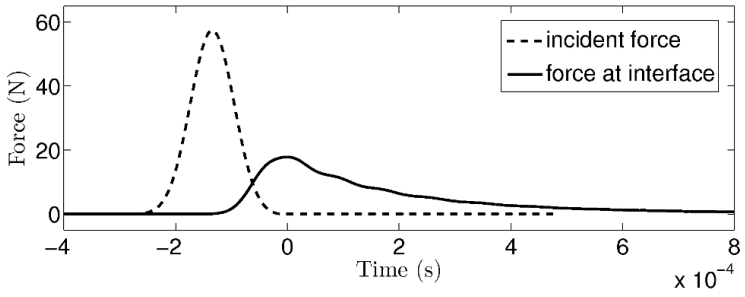

(a) numerical results

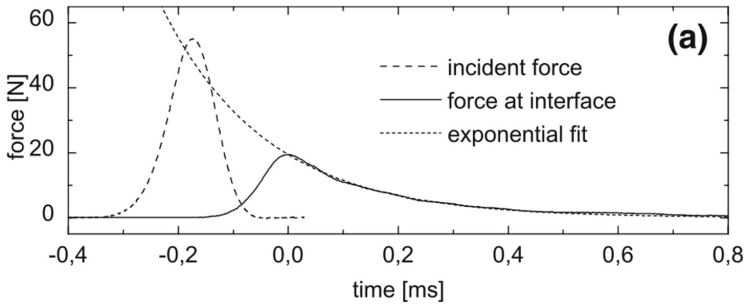

(b) experimental results

Figure 23: The incident force (at the contact before the interface) and the force at the interface obtained from the numerical simulation with $e_s = 1.0$ and $V_{in} = 0.31\ m/s$ (a) and the experimental test (b).

matched by the numerical results but for second SWT in [30] the numerical simulations give a significant discrepancy. When the local dissipation is introduced in the numerical simulations, both two SWTs are well matched by the numerical results. When comparing the incident force pulse and the force pulse at the interface obtained from the numerical simulations to the experimental ones, it is observed that the numerical simulations with or without local dissipation overestimate the incident amplitude and underestimate the ratio of the amplitude at the interface to the incident amplitude.

7 Interaction of two solitary waves in monodisperse chains

We now turn our attention to the interaction of two solitary waves in monodisperse chains. This problem has been numerically investigated in [33] and in [16] and experimentally investigated in [32]. In [32], the authors have conducted experimental tests on two monodisperse chains composed of 25 of 26 steel beads of radius $R = 13\ mm$ (odd chain and even chain). Bead properties are as follows: density $\rho = 7780\ kg/m^3$, Young's modulus $E = 203\ GPa$ and Poisson ratio $\nu = 0.3$. Initially the beads in the chains barely touch each other. Then the chains are impacted simultaneously at the two ends by two identical strikers of

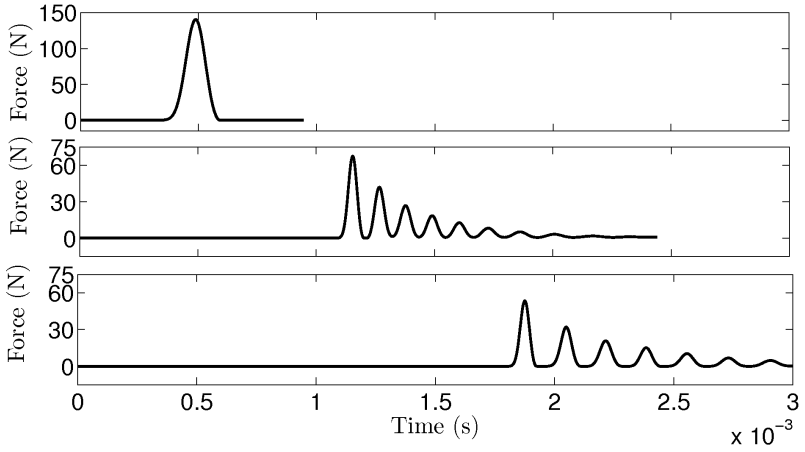

Figure 24: Solitary wave and solitary wave trains in stepped chains obtained from the numerical simulations. First row corresponds to the force recorded at the end of a monodisperse chain composed of 7 beads of radius $R_1 = 13\ mm$. Second (resp. last) row corresponds to the force recorded at the end of a stepped chain composed of 7 beads of radius $R_1 = 13\ mm$ and 25 (resp. 50) beads of radius $R_2 = 6.5\ mm$. The numerical simulations are performed with $e_s = 0.98$ and $V_{in} = 0.40\ m/s$.

radius $R_s = 4\ mm$. The contact force induced by the shocks is measured by the force sensors inserted inside beads 9 and 17.

7.1 Numerical simulations

We perform here numerical simulations of the experimental tests described above. The granular chains under consideration are identical to those in the experimental tests. In [32] the impact velocity V_{in} for each impactor and the coefficient of restitution e_s are not given. Therefore we proceed a fitting procedure to determine these parameters. In fact, we have the experimental data about the test for which only one solitary wave is generated along the same granular chains. This solitary wave is considered as "the reference solitary wave" and is shown in figure 2 in [32]. Based on this reference solitary wave, we can determine the impact velocity and coefficient of restitution by varying them in such a way that the amplitude of the reference solitary wave when it passes through beads 9 and 17 is reproduced in the chains of 25 and 26 beads. From the fitting procedure, we obtain a restitution coefficient $e_s = 0.93$ for both chains and an impact velocity $V_{in} = 0.31 m/s$ for the chain of 25 beads and $V_{in} = 0.40 m/s$ for the chain of 26 beads. Table 1 shows the force amplitude at the right contact of bead 9 and at the left contact of bead 17 obtained from the numerical simulation for the two chains with the parameters obtained from the fitting procedure, compared to the experimental data. It is worth mentioning that the coefficient of restitution obtained here is a little lower than that obtained in section 5 ($e_s = 0.965$). This is likely due to the friction between the beads and the support in the experimental setup that is not taken into ac-

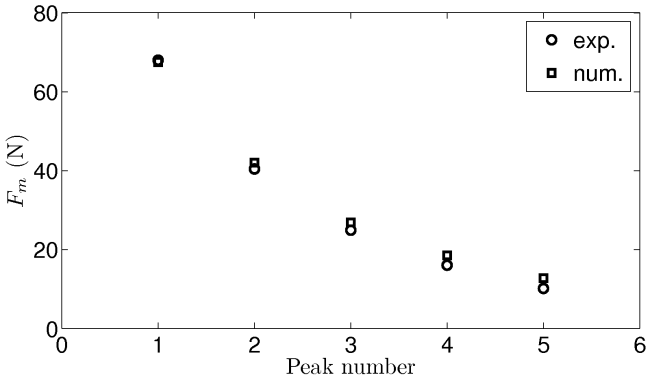

(a) with 25 beads of $R_2 = 6.5\ mm$

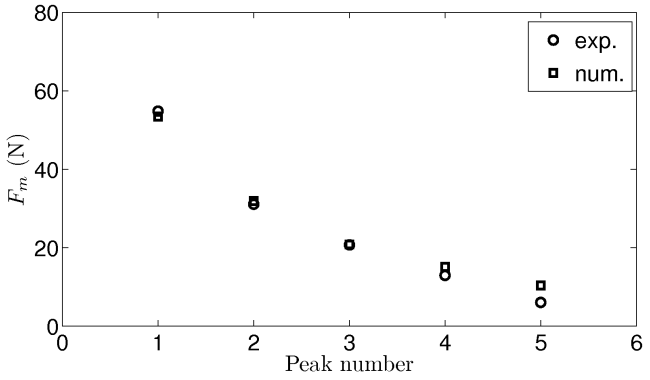

(b) with 50 beads of $R_2 = 6.5\ mm$

Figure 25: Force at the peaks in the solitary wave train obtained from the numerical simulations, compared to the experimental data for the solitary wave train at the end of the stepped chain with 25 beads of $R_2 = 6.5\ mm$ (a) and 50 beads of $R_2 = 6.5\ mm$ (b). The numerical simulations are performed with $e_s = 0.98$ and $V_{in} = 0.40\ m/s$.

count in the LZB-complementarity model without friction. In fact, in the latter case the fitting procedure is applied over a length of about 8 beads whereas the length in the former case is about 17 beads. Thus the solitary wave travels a longer distance in the former case than in the latter case, and so the dissipation due to friction might play a more important role in the former case than in the latter case. For the numerical simulations, the bistiffness compliance contact model is considered and the step size is $\Delta P = 10^{-6}\ N.s$.

7.2 Numerical results

The two solitary waves before and after the interaction between them obtained from the numerical simulations for the odd and even chains are shown in figure 28a, compared to the experimental data shown in figure 28b. The solitary wave that is initiated at the left end (resp. right) of the chains is called the left-hand

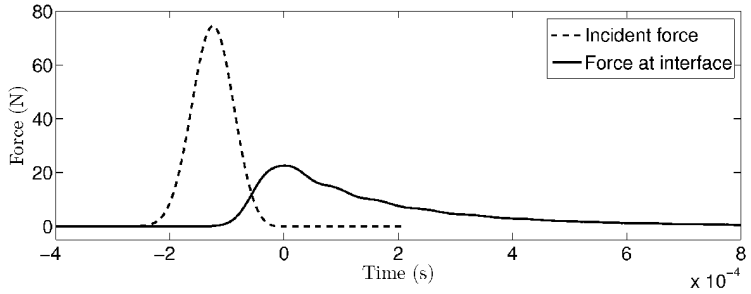

Figure 26: The incident force (at the contact before the interface) and the force at the interface obtained from the numerical simulations with $e_s = 0.98$ and $V_{in} = 0.40\ m/s$

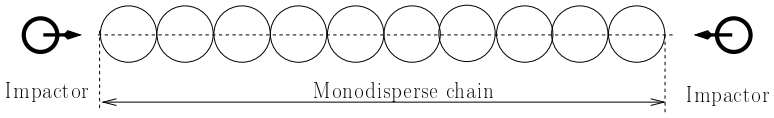

Figure 27: Numerical test of solitary waves interaction in a monodisperse chain. Two solitary waves are initiated simultaneously at both ends of the chain by two indentical impactors.

Chain of	Parameters	Numerical data	Experimental data
25 beads	$V_{in} = 0.31\ m/s$	$F_m(n = 9) = 8.5N$	$F_m(n = 9) = 8.2N$
	$e_s = 0.93$	$F_m(n = 17) = 6.5N$	$F_m(n = 17) = 6.2N$
26 beads	$V_{in} = 0.40\ m/s$	$F_m(n = 9) = 11.6N$	$F_m(n = 9) = 11.1N$
	$e_s = 0.93$	$F_m(n = 17) = 8.8N$	$F_m(n = 17) = 9.2N$

Table 1: Force amplitude at the right contact of bead $n = 9$ and the left contact of bead $n = 17$ obtained from the numerical simulations with monodisperse chains of 25 and 26 beads, compared to the experimental data. The parameters used for each chain are shown in the second column of this table.

(resp. right-hand) side travelling wave (LSTW, resp. RSTW). It is shown that on the whole the numerical simulations reproduce rather well what happens when two solitary waves collide in a monodisperse chain. For the odd chain, LSTW arrives to the bead 17 with a time delay $\Delta = 35.5\mu s$ with respect to the reference solitary wave, close to the value $\Delta = 32.5\mu s$ obtained from the experimental test. The amplitude of LSTW at this instant is about 7.0 N, compared to the experimental value of 6.2 N. SSWs with small amplitude are not clearly observed for this odd chain in the numerical simulations and as weel in the experimental tests (the amplitude of the SSWs is very small). In the other hand, we can observe clearly two SSWs after the collision of the two solitary waves LSTW and RSTW for the even chain in the numerical simulations and in the experimental tests. The amplitude of the SSWs (about 0.32N) is smaller

than the experimental value (about 1N). This means that the SSWs in the case that two SWs collide in an even chain is stronger than in an odd chain. This observation has been confirmed in [33]. The time delay of LSTW with respect to the reference SW for the even chain is about $33.7\mu s$, close to the experimental value of $31.7\mu s$. A discrepancy between the numerical simulations and the experimental tests can be observed when comparing the amplitude of LSTW after collision for the even chain. In the numerical simulations the amplitude of LSTW after collision is close to that of the reference SW but in the experimental tests the former is significantly lower than the latter. In [32] the authors have also performed numerical simulations based on the second order equation of motion, the Hertz contact model. The local dissipation at the contacts points is taken into account by using a nonlinear viscoelastic solid model [36]. The numerical results obtained from this simulation is shown 29. When comparing the numerical results obtained from the numerical simulations performed with the LZB-complementarity model which takes into account the local dissipation by using the energetic restitution coefficient (shown in 28a) and the numerical results in [32] (shown in 29), we can see that the first ones match better the experimental data than the second ones. Furthermore, the SSWs are more clearly observed in the simulations with the LZB-complementary model than in the simulations in [32].

7.3 Conclusions

We investigate in this section the interaction between two solitary waves (SWs) propagating in monodisperse chains by performing the numerical simulations and compare the numerical results obtained to the experimental data available in [32]. It is found out that the numerical simulations with the LZB-complementarity multiple impact model are able to well reproduce the effects when two SWs collide. The time delay that results from the collision of two SWs and the amplitude of the SWs after collision found in the experimental tests are well matched by the numerical results. The secondary solitary waves (SSWs) that are generated after collision can be observed in the numerical tests for the monodisperse chains composed of an even number of beads. However, these SSWs are significantly smaller than those observed in the experimentals tests. The numerical simulations with LZB-complementarity multiple impact model give the results that match better the experimental data than the numerical simulations performed in [32] that take into account the local dissipation by a nonlinear viscoelastic solid model.

8 General conclusions

In this work, we present the numerical simulations of impact dynamics for granular chains performed with the LZB-complementarity multiple impact model that is implemented with the event-driven numerical scheme in the SICONOS platform. Different kinds of granular chains are considered: monodisperse chains, tapered chains, stepped chains. We focus on analyzing the impact process in these granular chains by striking them at one end or at both ends. We also compare the numerical results obtained to the experimental results presented in [19], [18], [30], [32]. In some cases, some parameters necessary to perform

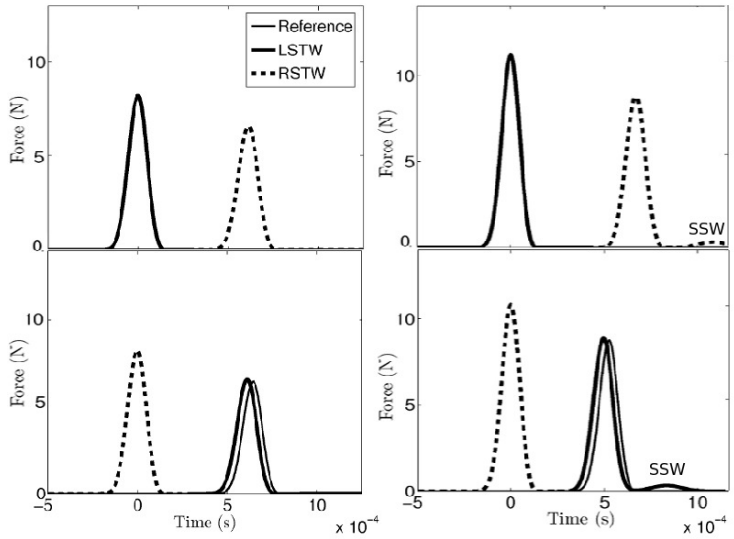

(a) numerical result

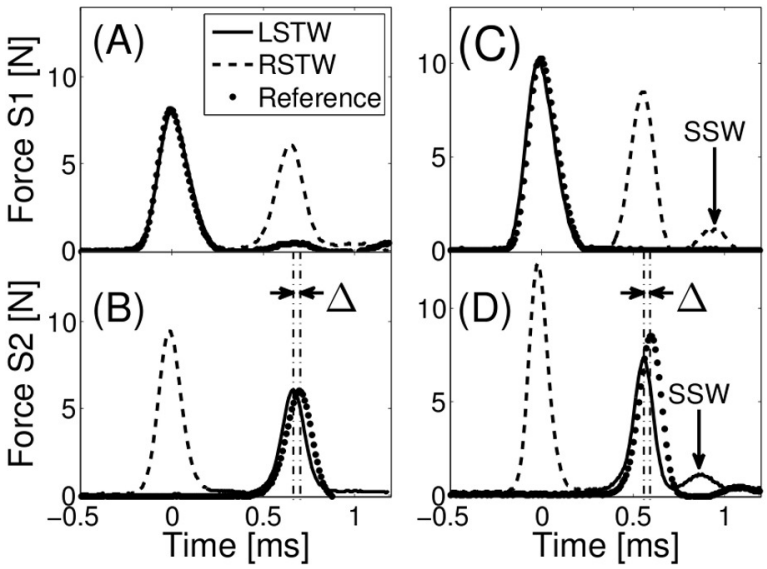

(b) experimental result

Figure 28: Interaction of two solitary waves in monodisperse chains obtained from (a) the numerical simulations and (b) the experimental tests. Left and right columns correspond to the chain of 25 and 26 beads, respectively. In each column, the top panel shows the force felt at the right contact of bead 9 and the bottom panel shows the force felt at the left contact of bead 17. LSTW is the left-hand side travelling wave (initiated on the left of the chain) and RSTW is the right-hand side travelling wave (initiated on the right of the chain).

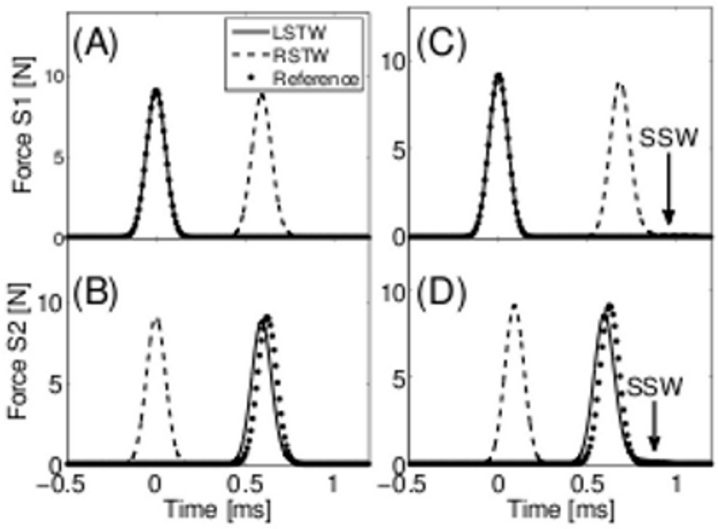

Figure 29: Numerical results presented in [32].

numerical simulations (impact velocity, restitution coefficient) are not explicitly given in the experimental tests. Therefore, we apply the fitting procedure to the experimental data available for some experimental tests to determine these parameters. Then we use the parameters obtained for another tests. The comparison between the numerical results and the experimental results shows that the numerical simulations with LZB-complementarity multiple impact model are able to predict well what happens during the impact process for granular chains and that the numerical results match well the experimental results. More precisely, the following conclusions can be drawn:

- the outcomes of the impact process for tapered chains, obtained from the numerical simulations are in very good agreement with the experimental data shown in [19]. Moreover, the propagating force pulse presented in [18] are well reproduced by the numerical simulations. However, some discrepancies are found between the numerical and experimental results, in particular in terms of wave speed and tail impulses. This might be due to partly the limitation of the measurement technique used in the experimental tests. Analyzing the numerical results points out that the measurement technique used in [18] using a wall sensor might be not suitable to investigate the wave propagating in tapered chains as the wall sensor disturbs their boundary conditions.

- the formation and propagation of a solitary wave train (SST) in stepped chains are well reproduced by the numerical simulations. For the simulations without local dissipation, the SST remains constant when travelling, which leads to some discrepancies between the numerical results and the experimental results in [30]. When the local dissipation is taken into account by using the energetic restitution coefficient, the SST is attenuated when travelling and the experimental data is better reproduced.

- the interaction effects between two solitary waves (SWs) in monodisperse chains are put in evidence by the numerical simulations. The interaction between two SWs leads to a delay time of each SW compared to the case when only one SW propates and a formation of secondary solitary waves (SSWs) with a small amplitude. In the numerical simulations, the SSWs are clearly observed in a monodisperse chain composed of an even number of beads. However, the amplitude of these SSWs obtained in the numerical tests are significatly lower than in the experimental tests. The numerical simulations with LZB-complementarity multiple impact model match better the experimental data in [32] than the numerical simulations performed in the same paper.

The above results demonstrate that the numerical simulations with LZB-complementarity multiple impact model are able to simulate impact dynamics of granular chains, strictly speaking and of mechanical systems of multiple rigid bodies, generally speaking. With the LZB-complementarity multiple impact model, the local dissipation at contact points during the collisions between contacting bodies can be consistently taken into account by using the energetical constraint. Introducing the local dissipation, the numerical results obtained with this impact model match better experimental data.

A Numerical scheme for LZB-complementarity model

A.1 Algorithm

The numerical scheme to solve the impact problem with LZB-complementarity multiple impact model consists in first discretizing the principal impulse P (the dump integration variable) into steps 0, 1, ..., N of size ΔP (a step k goes from instant P_k to instant $P_{k+1} = P_k + \Delta P$) and then in applying the algorithm described in 1, 2 and 3.

A.2 Convergence of the algorithm

In order to evaluate the convergence of a numerical solution, we can compare the solution obtained from the simulation performed with a given step size $\Delta P = h$ to the solution obtained with a smaller step size (for example a half of the latter step size). If the two solutions do not greatly differ from each other, we may consider that the solution obtained with the step size $\Delta P = h$ converges to the solution of the multiple impact problem that we are simulating. The difference between the solutions (that can be described in terms of velocity of the balls during the simulation) obtained with two different values of the step size (h and $h/2$) can be quantified by a discrepancy quantity defined as follows:

$$\Phi_h(P) = \frac{\|\dot{\boldsymbol{q}}_h(P) - \dot{\boldsymbol{q}}_{h/2}(P)\|}{\|\dot{\boldsymbol{q}}_{h/2}(P)\|}, \tag{46}$$

where $\dot{\boldsymbol{q}}_h(P)$ and $\dot{\boldsymbol{q}}_{h/2}(P)$ are respectively the vectors of the generalized velocity of the considered system at instant P during the simulation (P is the dumb

integration variable considered in the simulation) obtained with two values of the step size h and $h/2$. The symbol ($\|.\|$) represents the maximum norm.

We can also evaluate the convergence of the numerical solution obtained with a step size $\Delta P = h$ by computing another discrepancy quantity in terms of post-impact velocity as follows:

$$\Phi_h^+ = \frac{\|\dot{\boldsymbol{q}}_h^+ - \dot{\boldsymbol{q}}_{h/2}^+\|}{\|\dot{\boldsymbol{q}}_{h/2}^+\|}, \tag{47}$$

where $\dot{\boldsymbol{q}}_h^+$ and $\dot{\boldsymbol{q}}_{h/2}^+$ are respectively the vectors of the generalized post-impact velocity of the considered system, obtained with two values of the step size h and $h/2$.

The numerical solution obtained from the simulation with a step size h is considered to be convergent to the solution of the multiple impact problem if the following criteria are satisfied:

$$\Phi_h(P) \leq \epsilon \quad \forall P, \tag{48}$$

$$\Phi_h^+ \leq \epsilon^+, \tag{49}$$

where ϵ and ϵ^+ are precisions for the numerical results in terms of the evolution of the system during the impact and of the outcome of the impact, respectively. The choice of the values for ϵ and ϵ^+ depends on the problem that we want to analyze. For example, a small value for ϵ^+ (resp. ϵ) should be used if we want to analyze the outcome of the impact (resp. if we want to analyze the evolution of the system during impact).

The choice of the step size ΔP constitues a crutial point in the numerical simulation with LZB-complementarity multiple impact model for a given granular chain. It is not an easy task since the choice of the step size ΔP depends on a lot of factors such as the geometry of the considered chain (size of the beads), the properties of the beads (density, Young modulus), the local dissipation (restitution coefficient), the impact velocity, etc. Therefore it is important to perform a convergence test using the precision criteria (48) and (49) to make sure that the solution obtained from the numerical simulation performed is convergent. In the following, we discuss the choice of the step size for three different granular chains considered as reference chains in order to give a guideline to choose a suitable step size when simulating the impact dynamics of granular chains with LZB-complementarity multiple impact model.

A.2.1 For a monodisperse chain of elastic beads

Let us now consider a monodisperse chain composed of 20 elastic beads of radius $R = 10\ mm$ ($e_s = 1.0$). The ball properties are: density $\rho = 7780\ kg/m^3$, Young modulus $E = 203\ GPa$ and Poisson coefficient $\nu = 0.3$. The chain is impacted by a striker identical to the beads in the chain with an impact velocity $V_s = 1\ m/s$. In the numerical simulations presented here, the bi-stiffness are considered.

Figure 31 presents the velocity of different beads in the chain versus the principal impulse P, obtained from the numerical simulations with different step sizes. It can be observed that the result obtained with $\Delta P = 1.0^{-4}$ differs

significantly from that obtained with $\Delta P = 1.0^{-5}$. This difference is small at the beginning of the simulation and then increases during the simulation, which is certainly due to the cumulative error during the integration. When the step size $\Delta P = 1.0^{-6}$ is used, the result obtained coincides almost with that obtained with $\Delta P = 1.0^{-5}$. This means that the numerical simulation converges when the step size is decreased.

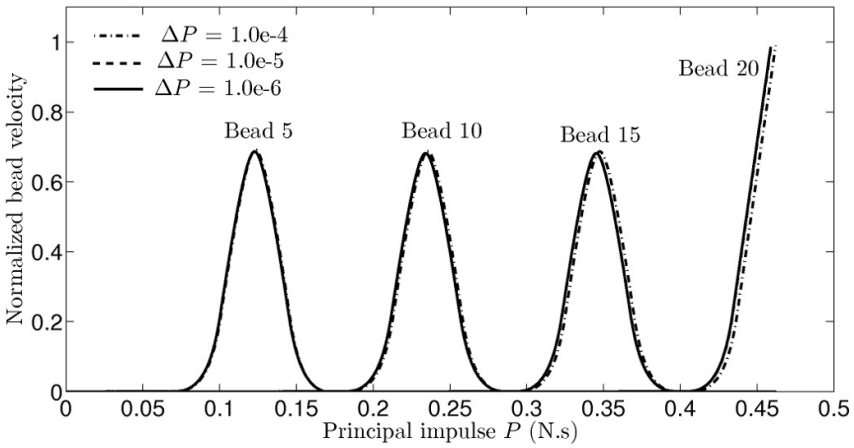

Figure 30: Velocity of different beads in the monodisperse chain with $e_s = 1.0$ during the numerical simulations with differents step size ΔP.

In figure 31, the discrepancy quantity Φ_h is plotted versus the principal impulse P during the simulations performed with different step sizes. For the step size $\Delta P = 10^{-4}$, the discrepancy Φ_h increases quickly and reaches an important value at the end of the simulation whereas it remains quite small for the step sizes $\Delta P = 10^{-5}$ and $\Delta P = 10^{-6}$.

Table 2 give some information about the numerical simulations with different step sizes such as the number of integration steps performed, computation time with a HP computer with four processors of 2.67 GHz, the maximum value of the discrepancy quantity Φ_h, the value of the discrepancy quantity Φ_h^+, and the convergence status evaluated with precisions $\epsilon = \epsilon^+ = 0.01$. We can see that for this monodisperse chain without dissipation, a step size ΔP about 1.0×10^{-5} allows to obtain a satisfactory solution.

Step size ΔP (N.s)	Number of steps	Computation time	max(Φ_h)	Φ_h^v	Convergence (Yes/No)
1.0×10^{-4}	4622	0.13 s	0.09	0.0046	No
1.0×10^{-5}	45913	0.79 s	0.008	0.0003	Yes
1.0×10^{-6}	458934	7.23 s	0.003	0.00015	Yes

Table 2: Information about the numerical simulations of the monodisperse chain with $e_s = 1.0$ and with different step sizes ΔP.

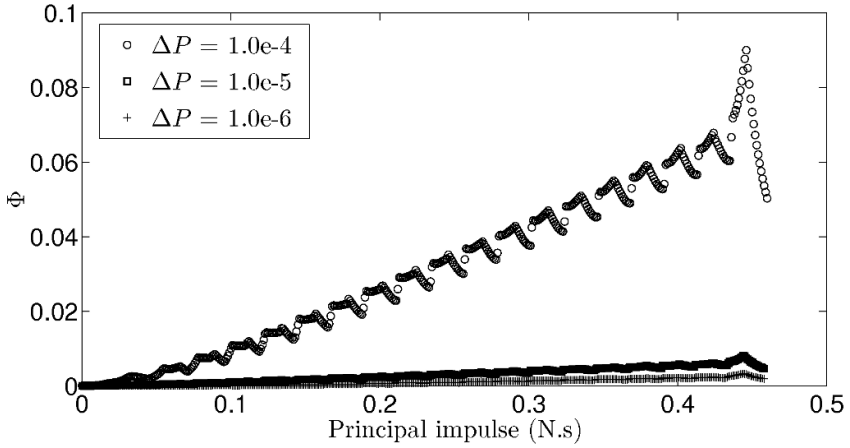

Figure 31: Discrepancy quantity Φ_h computed during the numerical simulation of the monodisperse chain with $e_s = 1.0$ with differents step size ΔP.

A.2.2 For a tapered chain of elastic beads

In this section we consider a tapered chain of 20 elastic beads ($e_s = 1.0$). The radii of the beads in the chain progressively decrease such that $R_{i-1} = (1-q)R_i$ with $q = 5\%$ being the tapering factor. First bead in this tapered chain and other parameters are identical to those for the monodisperse chain considered in section A.2.1. We performed numerical simulations of this tapered chain with different step sizes ΔP. As can be seen in figure 34, the step sizes ΔP of 10^{-5} and 10^{-6} give close solutions. However, the discrepancy quantity $\max(\Phi_h) = 0.05$ for $\Delta P = 10^{-5}$ (see table 3), that is above the precision $\epsilon = 0.01$. As a consequence, the step size $\Delta P = 10^{-5}$ that is satisfactory for the monodisperse chain considered in section A.2.1 does not satisfy the precision critera (48) and (48). For this tapered chain, $\Delta P = 10^{-6}$ gives a satisfactory solution both in terms of the evolution of the system during the impact process and in terms of the outcome of the impact process.

Step size ΔP (N.s)	Number of steps	Computation time	$\max(\Phi_h)$	Φ_h^+	Convergence (Yes/No)
1.0×10^{-5}	22331	0.42 s	0.05	0.002	No
1.0×10^{-6}	223001	3.76 s	0.006	0.00007	Yes

Table 3: Information about the numerical simulations performed for the tapered chain of elastic balls with different step sizes.

A.2.3 For a monodisperse chain of inelastic beads

We consider now the same monodisperse chain as the one considered in section A.2.1 but the local dissipation is introduced by using a restitution coefficient $e_s = 0.6$. For such a strongly dissipative chain, the velocity of different

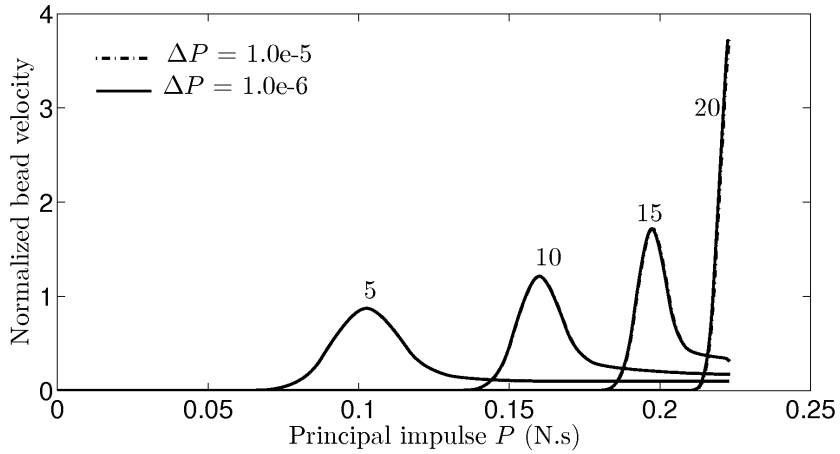

Figure 32: Velocity of different beads during the numerical simulations performed for the tapered chain of elastic balls with differents step sizes ΔP.

beads during the numerical simulations performed with different step sizes ΔP is shown in figure 33. As a whole, the solutions obtained with the step sizes $\Delta P = 10^{-5},\ 10^{-6},\ 10^{-7}$ are quite close. However, a significant discrepancy can be observed at the end of the simulations when making a zoom on figure 33 at the end of the curves, as illustrated in figure 33. In fact, in the presence of the dissipation at the contact points, dynamics of the chain becomes strongly oscilating with a high frequency. At the end of the impact process, oscilations become faster and have a small amptitude. Therefore it is not easy to integrate properly this kind of oscillations even when the step size is small. Although the evolution of the system at the end of the impact process is not convergent when the step size is decreased from 10^{-6} to 10^{-7}, the outcome of the simulations is convergent. Indeed, the difference between the post-impact velocities of the beads obtained with $\Delta P = 10^{-6}$ and those obtained with $\Delta P = 10^{-7}$ is smaller than 1%. Table 4 shows the discrepancy quantities for different step sizes. It can be seen that the precision criterion (49) is satisfied with both step sizes $\Delta P = 10^{-6}$ and $\Delta P = 10^{-7}$ but not the precision criterion (48). For this kind of chain, neglecting the oscilations with small ampltitude and high frequency at the end of the impact process does not change the main evolution of the system during impact process and the output of the simulation. A step size ΔP about 10^{-6} gives satisfactory solution.

B Algorithm for event-driven scheme

For the event-driven scheme, we first discretize the time interval $[0, t_f]$ into steps of size Δt. A step k goes from instant t^k to instant $t^{k+1} = t^k + \Delta t$. Then the following algorithm is applied.

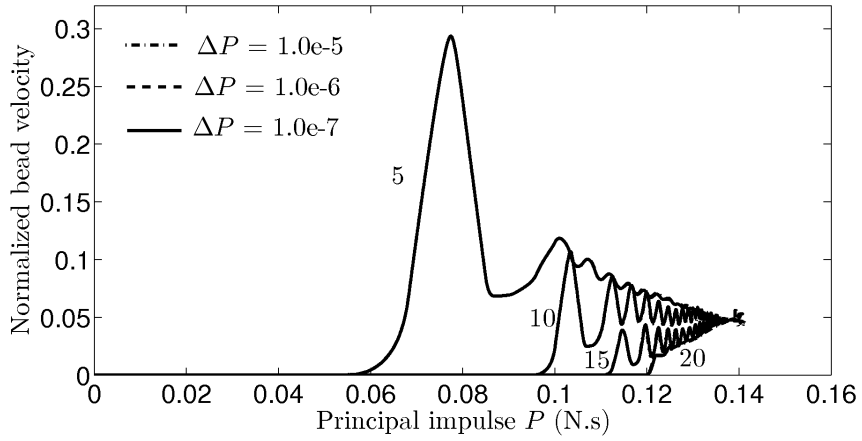

Figure 33: Velocity of the beads during the numerical simulations performed for the monodisperse chain of inelastic balls ($e_s = 0.6$) with differents step sizes ΔP.

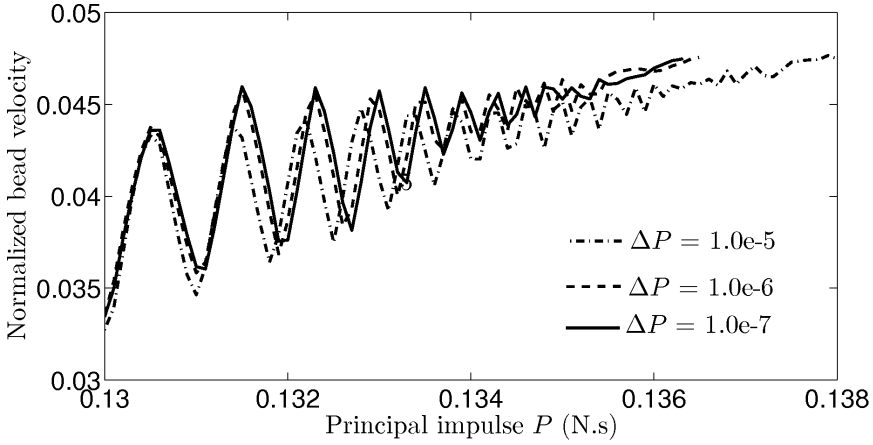

Figure 34: Velocity of bead 10 in the monodisperse chain with $e_s = 0.6$ at the end of the simulation with differents step sizse ΔP.

Step size ΔP (N.s)	Number of steps	Computation time	max(Φ_h)	Φ_h^+	Convergence (Yes/No)
1.0×10^{-5}	14139	0.40 s	0.13	0.07	No
1.0×10^{-6}	272754	4.76 s	0.013	0.0018	No
1.0×10^{-7}	1363111	23.06 s	0.03	0.002	No

Table 4: Information about the numerical simulations performed for the monodisperse chain of inelastic beads ($e_s = 0.6$) with $q = 5\%$ with different step sizes ΔP.

Algorithm 1 Algorithm for LZB-complementarity multiple impact model (part 1)

$P_* = 0$ ▷ *Principal impulse variable*
$t = 0$ ▷ *Time variable*
while $Termination = false$ **do** ▷ *while the multiple impacts not yet terminated*
  // For each step k, we compute δ_j^{k+1}, E_j^{k+1}, P_j^{k+1}, *values at the end of the step from* δ_j^k, E_j^k, P_j^k, *values at the beginning of the step*
  //========== Check the status of each contact at the beginning of step k
  for $j = 1 \rightarrow m$ **do**
    if $E_j^k = 0$ **then** ▷ *no potential energy at this contact*
      if $\dot{\delta}_j^k \leq 0$ **then**
        $flag_j^k = 0$ ▷ *contact does not enter into impact*
      else if $\dot{\delta}_j^k \geq 0$ **then**
        $flag_j^k = 1$ ▷ *contact begins the compression phase (included the repeating impact)*
      end if
    else if $E_j^k > 0$ **then** ▷ *potential energy is not zero at this contact*
      $flag_j^k = 2$ ▷ *contact is already in the impact process*
    end if
  end for
  //============ Check the termination condition for multiple impacts at the beginning of step k
  $Termination = true$
  for $j = 1 \rightarrow m$ **do**
    if $flag_j^k \neq 0$ **then**
      $Termination = false$
    end if
  end for
  //============ Select the primary contact (*) at the beginning of step k
  $* = 1$
  if $max(E_j^k)_{j=1,\ldots,m} = 0$ **then** ▷ *in this case, the primary contact is selected according to the relative velocity at contact points*
    $PrimaContactVel = true$
    for $j = 1 \rightarrow m$ **do**
      if $\dot{\delta}_*^k < \dot{\delta}_j^k$ **then**
        $* = j$
      end if
    end for
  else if $max(E_j^k)_{j=1,\ldots,m} > 0$ **then** ▷ *in this case, the primary contact is selected according to the potential energy at contact points*
    $PrimaContactVel = false$
    for $j = 1 \rightarrow m$ **do**
      if $E_*^k < E_j^k$ **then**
        $* = j$
      end if
    end for
  end if

Algorithm 2 Algorithm for LZB-complementarity multiple impact model (part 2)

41: //==========*Apply the distributing rules* (12), (13) *and* (11) *to compute the change of the impulse* δP_j^k at each contact
42: **if** $PrimaContactVel = true$ **then** ▷ *if the primary contact is selected according to the relative velocity at contact points*
43: **for** $j = 1 \rightarrow m$ **do**
44: $\delta P_j^k = \frac{K_j}{K_*}\left(\frac{\dot{\delta}_j^k}{\dot{\delta}_*^k}\right)^{\eta}\Delta P$
45: **end for**
46: **else**▷ *if the primary contact is selected according to the potential energy at contact points*
47: **for** $j = 1 \rightarrow m$ **do**
48: **if** $flag_j^k = 0$ **then**
49: $\delta P_j^k = 0$
50: **else if** $flag_j^k = 1$ **then**
51: $\delta P_j^k = \frac{K_j}{K_*}\left(\frac{\dot{\delta}_j^k \Delta P}{E_*^k}\right)^{\eta}$
52: **else if** $flag_j^k = 2$ **then**
53: $\delta P_j^k = \left(\frac{K_j}{K_*}\right)^{\frac{1}{1+\eta}}\left(\frac{E_j^k}{E_*^k}\right)^{\frac{\eta}{\eta+1}}$
54: **end if**
55: **end for**
56: **end if**
57: //========== *Compute the relative velocity at the end of step* k *by applying the difference formulation to* (8)
58: **for** $j = 1 \rightarrow m$ **do**
59: $\dot{\delta}_j^{k+1} = \dot{\delta}_j^k + (H_c)_{jl}\delta P_l^k$
60: **end for**
61: //========== *Compute the potential energy for the end of the step by applying the numerical integration to* (15), (16)
62: **for** $j = 1 \rightarrow m$ **do**
63: **if** MonoStiffnessModel **then** ▷ *For Mono-stiffness compliance model*
64: $E_j^{k+1} = E_j^k + \frac{\dot{\delta}_j^k + \dot{\delta}_j^{k+1}}{2}\delta P_j^k$
65: *//Determine the work done during the compression phase* $W_{c,j}$
66: **if** $(\dot{\delta}_j^k \geq 0,\ \dot{\delta}_j^{k+1} < 0)$ **then** ▷ *transition from the compression to expansion phase*
67: $W_{c,j} = E_j^k$
68: **end if**
69: *//Check the energetic constraint*
70: **if** $(\dot{\delta}_j^k < 0,\ E_j^k \leq (1 - e_{s,j}^2)W_{c,j})$ **then** ▷ *during the expansion phase and the energetic constraint is satisfied*
71: $E_j^k = 0$ ▷ *discard the potential energy*
72: **end if**

Algorithm 3 Algorithm for LZB-complementarity multiple impact model (part 3)

else if BiStiffnessModel **then** ▷ *For Bi-stiffness compliance model*
  if $\dot{\delta}_j^k \geq 0$ **then** ▷ *contact located in the compression phase*
    $E_j^{k+1} = E_j^k + \dfrac{\dot{\delta}_j^k + \dot{\delta}_j^{k+1}}{2}\delta P_j^k$
  else if $\dot{\delta}_j^k < 0$ **then** ▷ *contact located in the expansion phase*
    $E_j^{k+1} = E_j^k + \dfrac{1}{e_{s,j}^2}\dfrac{\dot{\delta}_j^k + \dot{\delta}_j^{k+1}}{2}\delta P_j^k$
  end if
end if
end for
//============== *Compute the force at the contact points using (17)*
for $j = 1 \rightarrow m$ **do**
  if $E_j^k = 0$ **then** ▷ *the potential energy at this contact is zero*
    $\lambda_j^k = (1+\eta)^{\frac{\eta}{\eta+1}} K_j^{\frac{1}{1+\eta}} (\dot{\delta}_j^k \delta P_j^k)^{\frac{\eta}{\eta+1}}$
  else ▷ *the potential energy at this contact is not zero*
    $\lambda_j^k = (1+\eta)^{\frac{\eta}{\eta+1}} K_j^{\frac{1}{1+\eta}} (E_j^k)^{\frac{\eta}{\eta+1}}$,
  end if
end for
//============== *Compute the principal impulse P^* and the time t during the impact process*
$P_* = P_* + \delta P_*^k$
$t = t + \frac{\delta P_*^k}{\lambda_*^k}$
end while

Algorithm 4 Algorithm for the event-driven scheme

while $t^k \leq t^f$ **do**
//=============== Check if some contacts are activated or not at instant t^k
if $I_c^k = \emptyset$ **then**
$status^k = 0$ ▷ *Free flight motion*
else
$status^k = 1$ ▷ *Some contacts are activated*
end if
//=============== Integrate up to the next instant t^{k+1}
if $status^k = 0$ **then**
Integrate the DAE (20) up to the next instant t^{k+1}. During this integration, the ODE solver will perfom a root finding of functions $\delta_j(t) = 0 \quad \forall j \in I$. If a root is found at an instant $t^* \leq t^{k+1}$, the solver throws an integer $Istate = 1$ and $Istate = 0$ if otherwise.
if $Istate = 1$ **then** ▷ *A nonsmooth even is found*
Add a new event at instant t^*
Set $t^{k+1} = t^*$
$ProcessNSEvent = true$ ▷ *the added event needs to be processed*
end if
else if $status^k = 1$ **then**
Integrate the the system LCP at acceleration level (26) + ODE (25) up to the next instant t^{k+1}. During this integration, the ODE solver will perfom a root finding of functions $\delta_j(t) = 0 \quad \forall j \in I \setminus I_s^k$ and $\lambda_j(t) = 0 \quad \forall j \in I_s^k$. If a root is found at an instant $t^* \leq t^{k+1}$, the solver throws an integer $Istate = 1$ and $Istate = 0$ if otherwise.
if $Istate = 1$ **then**
Add a new event at instant t^*
Set $t^{k+1} = t^*$
$ProcessNSEvent = true$ ▷ *the added event needs to be processed*
end if
end if
//=============== Update the index sets
Update the index sets with the algorithm described in 5
//=============== Process nonsmooth events if they are found
if $ProcessNSEvent = true$ **then**
Process the nonsmooth events added with the algorithm described in 6
end if
end while

Algorithm 5 Algorithm to update the index sets at instant t_{k+1}

for $j \in I^{k+1}$ **do**
  //=============== First, update the index set I_c^{k+1}
  if $j \ni I_c^{k+1}$ **then** ▷ *if* j *is not in the index set* I_c^{k+1}
    if $\delta_j^{k+1} = 0$ **then**
      Insert j into I_c^{k+1}
    end if
  else ▷ *if* j *is already in the index set* I_c^{k+1}
    if $\delta_j^{k+1} > 0$ **then**
      Remove j from I_c^{k+1}
    end if
  end if
  //=============== Update the index set I_s^{k+1}
  if $j \in I_c^{k+1}$ **then** ▷ *if* j *is in the index set* I_c^{k+1}
    if $j \ni I_s^{k+1}$ **then** ▷ *if* j *is not in the index set* I_s^{k+1}
      if $\dot{\delta}_j^{k+1} = 0$ **then**
        Insert j into I_s^{k+1}
      end if
    else ▷ *if* j *is already in the index set* I_s^{k+1}
      if $\dot{\delta}_j^{k+1} \neq 0$ **then**
        Remove j from I_s^{k+1}
      end if
    end if
  else ▷ *if* j *is not in the index set* I_c^{k+1}
    Remove j from I_s^{k+1}
  end if
end for

Algorithm 6 Algorithm to process the nonsmooth events

//=============== If impact occurs at some contact points
if $I_c^{k+1} \setminus I_s^{k+1} \neq \emptyset$ **then**
  Solve the impact problem using the LZB-complementarity multiple impact model with the algorithm described in 1 and 2
  Update the index sets I_c^{k+1} and I_s^{k+1} with the algorithm described in 5
  Make sure that $I_c^{k+1} \setminus I_s^{k+1} = \emptyset$
end if
//=============== If detachment occurs at some contact points
if $I_s^{k+1} \neq \emptyset$ **then**
  Solve LCP at acceleration level (26)
  // Update the index set I_s^{k+1} *with values* λ_j^{k+1} *and* $\ddot{\delta}_j^{k+1}$ *obtained from the resolution of LCP* (26)
  for $j \in I_s^{k+1}$ **do**
    if $(\ddot{\delta}_j^{k+1} > 0, \lambda_j^{k+1} = 0)$ **then**
      Remove j from I_s^{k+1}
    end if
  end for
end if

References

[1] Brogliato B. (1999) Nonsmooth Mechanics, 2nd Ed., Springer Verlag London.

[2] Nesterenko V.F. (2001) Dynamics of Heterogeneous Materials, Springer-Verlag, NewYork.

[3] Darboux G. (1880) Etude géométrique sur les percussions et les chocs des corps, *Bulletin des Sciences Mathématiques et Astronomiques*, deuxième série, tome 4:126-160.

[4] Keller J.B. (1986) Impact with friction, *ASME Journal of Applied Mechanics*, **53**:1-4.

[5] Ceanga V., Hurmuzlu Y., (2001) A new look at an old problem: Newton's cradle. *ASME J. Appl. Mech.*, **68**(4):575-583.

[6] Daraio C., Nesterenko V.F., Herbold E.B., Jin S. (2006) Energy Trapping and Shock Disintegration in a Composite Granular Medium, *Phys. Rev. Lett.*, **96**(058002).

[7] Ponson L., Boechler N., Lai Y.M., Porter M.A., Kevrekidis P.G., Daraio C. (2010) Nonlinear waves in disordered diatomic granular chains, *Phys. Rev. E*, **82**(021301).

[8] Porter M.A., Daraio C., Szelengowicz I., Herbold E.B., Kevrekidis P.G. (2009) Highly nonlinear solitary waves in heterogeneous periodic granular media, *Physica D*, doi:10. 1016/j.physd.2008.12.010.

[9] Job S., Santibanez F, Tapia F., Melo F. (2009) Wave localization in strongly nonlinear Hertzian chains with mass defect, *Phys. Rev. E*, **80**(025602(R)).

[10] S. Dorbolo, D. Volfson, L. Tsimring, A. Kudrolli. (2005) Dynamics of a bouncing dimer, *Physical Review Letters*, **95**(4): art. no 044101, 1-4.

[11] E. Falcon, C. Laroche, S. Fauve, S. Coste. (1998) Collision of a 1-D column of beads with a wall, *European Physical Journal B*, **5**(1): 111-131.

[12] M. Gharib, A. Celik, Y. Hurmuzlu. (2011) Shock absorption using linear particle chains with multiple impacts, *ASME Journal of Applied Mechanics*, **78**: 031005-1—031005-9.

[13] C. Glocker. (2004) Concepts for modeling impacts without friction, *Acta Mechanica*, **168**: 1-19.

[14] Job S., Melo F., Sokolow A., Sen S. (2005) How Hertzian solitary waves interact with boundaries in a 1D granular medium, *Phys. Rev. Lett.*, **94**(178002).

[15] C. Liu, Z. Zhao, B. Brogliato. (2008) Frictionless multiple impacts in multibody systems: Part I. Theoretical framework, *Proceedings of the Royal Society A, Mathematical, Physical and Engineering Sciences*, **464** (2100):3193-3211, December.

[16] C. Liu, Z. Zhao, B. Brogliato. (2008) Energy dissipation and dispersion effects in a granular media, *Physical Review E*, **78**(3): 031307, September.

[17] C. Liu, Z. Zhao, B. Brogliato. (2009) Frictionless multiple impacts in multibody systems: Part II. Numerical algorithm and simulation results, *Proceedings of the Royal Society A, Mathematical, Physical and Engineering Sciences*, **465**(2101): 1-23, January.

[18] Melo F., Job S., Santibanez F., Tapia F. (2006) Experimental evidence of shock mitigation in a Hertzian tapered chain, *Phys. Rev. E*, **73**(041305).

[19] Nakagawa M., Agui J.H., Wu D.T., Extramiana D.V. (2003) Impulse dispersion in a tapered granular chain, *Granular Matter*, **4**:167-174.

[20] Nesterenko V. F. (2001) Dynamics of heterogeneous materials, *Springer-Verlag, New York*.

[21] L. Paoli. (2005) Continuous dependence on data for vibro-impact problems, *Math. Models Methods Appl. Sci. (M3AS)*, **15** (1): 1-41.

[22] M.D. Payr. (2008) An experimental and theoretical study of perfect multiple contact collisions in linear chains of bodies, PhD Thesis no 17808, ETH Zurich.

[23] S. Sen, J. Hong, J. Bang, E. Avalos, R. Doney. (2008) Solitary waves in the granular chain, *Physics Reports*, **462**:21-66.

[24] H. Zhang, B. Brogliato (2011) The planar rocking block: analysis of kinematic restitution laws, and a new rigid-body impact model with friction, INRIA Research Report RR-7580, March 2011, http://hal.inria.fr/inria-00579231/en/.

[25] Z. Zhao, C. Liu, B. Brogliato. (2009) Planar dynamics of a rigid body system with frictional impacts. II. Qualitative analysis and numerical simulations, *Proceedings of the Royal Society A, Mathematical, Physical and Engineering Sciences*, **465** (2107):2267-2292, July.

[26] Stronge W.J., (2000) Impact Mechanics. *Cambridge University Press*.

[27] Lazaridi A.N., Nesterenko V.F., (1985) Observation of a new type of solitary waves in a one-dimensional granular medium, *J. Appl. Mech. Technol. Phys.*, **26**:405-408.

[28] Nesterenko V.F. (1994) Solitary waves in discrete media with anomalous compressibility and similar to "sonic vacuum", *Journal de Physique IV*, Colloque C8, supplément au Journal de Physique III, Volume 4, C8-729.

[29] Nesterenko V.F., Daraio C., Herbold E.B., Jin S. (2005) Anomalous wave reflection at the interface of two strongly nonlinear granular media, *Phys. Rev. Lett.*, **95**(158702).

[30] Job S., Melo F., Sokolow A., Sen S. (2007) Solitary wave trains in granular chains: experiments, theory and simulations, *Granular Matter*, **10**:13-20.

[31] Sokolow A., Bittle E.G., Sen S. (2007) Solitary wave train formation in Hertzian chains, *A Letters Journal Exploring The Frontiers Of Physics*, **77**(24002).

[32] Santibanez F., Munoz R., Caussarieu A., Job S., Melo F. (2011) Experimental evidence of solitary wave interaction in Hertzian chains, *arXiv:1102.3364v1*

[33] Ávalos E., Sen S. (2009) How solitary waves collide in discrete granular alignements, *Phys. Rev. E*, **79**, 046607.

[34] Hindmarsh A.C., (1983) ODEPACK, A Systematized Collection of ODE Solvers, in Scientific Computing, R. S. Stepleman et al. (Eds.), North-Holland, Amsterdam, 55-64.

[35] Acary V., Brogliato B. (2008) Numerical Methods for Nonsmooth Dynamical Systems: Application in Mechanics and Electronics, *Lecture Notes in Applied and Computational Mechanics*, vol 35, Springer-Verlag Berlin Heidelberg.

[36] Kuwabara G., Kono, K. (1987) Restitution coefficient in a collision between two spheres, *J.J. of Appl. Phys.*, **26**:1230-1233.

[37] Carretero-González R., Khatri D., Porter M.A., Kevrekidis P.G., Daraio C. (2009) Dissipative Solitary Waves in Granular Crystals, *Phys. Rev. Lett.*, **102**(024102).

[38] Rosas A., Romero A.H., Nesterenko V.F., Lindenberg K. (2007) Observation of Two-Wave Structures in Strongly Nonlinear Dissipative Granular Chains, *Phys. Rev. Lett.*, **98**(164301).

[39] Manciu M., Sen S., Hurd A.J. (2001) Impulse propagation in dissipative and disordered chains with power-law repulsive potentials, *Physica D.*, **157**:226-240.

[40] Wu D.T., (2002) Conservation principles in solitary impulse propagation through granular chains, *Physica A*, **315**:194-202.

[41] Pöschel T., Brilliantov N.V. (2001) Extremal collision sequences of particles on a line: Optimal transmission of kinetic energy, *Phys. Rev. E*, **63**(021505).

[42] Harbola U., Rosas A., Esposito M., Lindenberg K. (2009) Pulse propagation in tapered granular chains: an analytic study, *Phys. Rev. E*, **80**(031303).

[43] Harbola U., Rosas A., Romero A.H., Lindenberg K. (2010) Pulse propagation in randomly decorated chains, *Phys. Rev. E*, **82**(011306).

[44] Harbola U., Rosas A., Romero A.H., Esposito M., Lindenberg K. (2009) Pulse propagation in decorated granular chains: An analytical approach, *Phys. Rev. Lett.*, **80**(051302).

[45] Sen S., Manciu F.S., Manciu M. (2001) Thermalizing an impulse, *Physica A*, **299**:551-558.

[46] Sokolow A., Pfannes J.M.M., Doney R.L., Nakagawa M., Agui J.H., Sen S. (2005) Absorption of short duration pulses by small, scalable, tapered granular chains, *Applied Physics Letters*, **87**(254104).

[47] Pfannnes J., Sen S., Chakravarti S., Surve F.I. (2003) Energy absorption and recovery in tapered granular chains: small chains and low tapering, *Mat. Res. Soc. Symp. Proc.*, **759**.

[48] Doney R.L., Sen S. (2005) Impulse absorption by tapered horizontal alignments of elastic spheres, *Phys. Rev. E*, **72**(041304).

[49] Hascoë E., Herrmann H.J. (2000) Shock in non-loaded bead chains with impurities, *Eur. Phys. J. B.*, **14**(1):183-190.

Centre de recherche INRIA Grenoble – Rhône-Alpes
655, avenue de l'Europe - 38334 Montbonnot Saint-Ismier (France)

Centre de recherche INRIA Bordeaux – Sud Ouest : Domaine Universitaire - 351, cours de la Libération - 33405 Talence Cedex
Centre de recherche INRIA Lille – Nord Europe : Parc Scientifique de la Haute Borne - 40, avenue Halley - 59650 Villeneuve d'Ascq
Centre de recherche INRIA Nancy – Grand Est : LORIA, Technopôle de Nancy-Brabois - Campus scientifique
615, rue du Jardin Botanique - BP 101 - 54602 Villers-lès-Nancy Cedex
Centre de recherche INRIA Paris – Rocquencourt : Domaine de Voluceau - Rocquencourt - BP 105 - 78153 Le Chesnay Cedex
Centre de recherche INRIA Rennes – Bretagne Atlantique : IRISA, Campus universitaire de Beaulieu - 35042 Rennes Cedex
Centre de recherche INRIA Saclay – Île-de-France : Parc Orsay Université - ZAC des Vignes : 4, rue Jacques Monod - 91893 Orsay Cedex
Centre de recherche INRIA Sophia Antipolis – Méditerranée : 2004, route des Lucioles - BP 93 - 06902 Sophia Antipolis Cedex

Éditeur
INRIA - Domaine de Voluceau - Rocquencourt, BP 105 - 78153 Le Chesnay Cedex (France)
http://www.inria.fr
ISSN 0249-6399